Chapter 6:

Studies of Zeolite Encapsulated Ni(II) Schiff-Base Complexes: Improved Catalysis and Site Isolation

***Abstract**: Two series of zeolite encapsulated Ni(II) Schiff-base complexes e.g.{Ni(II) sal-1,2-phen and Ni(II) sal-1,3-phen series} have been synthesized in neat and encapsulated states and characterized by different characterization techniques such as XRD, SEM-EDS, BET, thermal analysis, XPS, IR, UV–Vis spectroscopy and magnetic studies. UV–Vis spectroscopy, XPS and magnetic studies all together reveal the structural modification of the guest complex and thereby, adaptation of electron density around the metal center upon encapsulation. However, encapsulation imposes structural alterations for these two series differently and hence, introduces a certain level of proficiency to these Ni(II) complexes as catalysts for phenol oxidation reaction. However, analysis of catalytic data emphasizes upon site isolation as major governing factor for the improved reactivity over the modified electron density around the metal center for phenol oxidation reaction when heterogeneous mode of catalysis is concerned.*

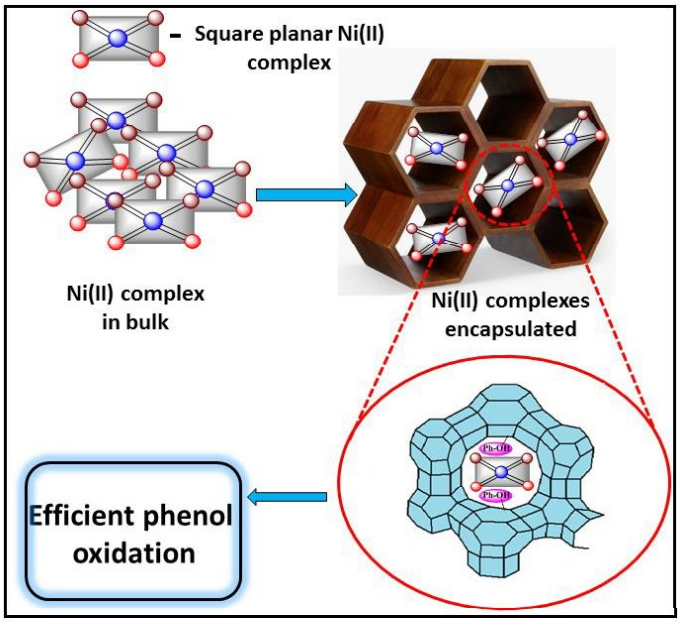

***S. Kumari** and S. Ray, Zeolite Encapsulated Ni(II) Schiff-Base Complexes: Improved Catalysis and Site Isolation, (*manuscript under revision*).

6.1 INTRODUCTION

Heterogenization of metal Schiff-base complexes has been attempted by immobilizing and encapsulating these homogeneous metal complex catalysts within the cavities of organic and inorganic supporting materials.[1-3] Among the all-supporting materials, zeolites deserve a special mention as zeolites indeed have considerably unique framework-architecture, thermal stability and ion exchange capability.[4, 5] The structures of zeolites are well-ordered with the building blocks organized in a regular array to form three-dimensional framework with regular cavities with large surface area and high stability.[6]

Transition metal-salophen complexes have wide range of applications in the area of material science. Metal complexes with salophen type ligand have drawn attention in the field of coordination chemistry due to their structural liability and sensitivity towards environment as a functional material.[7-9] The important characteristic of these complexes is associated with a tetradentate chelating system engendered by salophen ligand to form a stable complexes. These system act as proficient catalyst both in homogeneous and heterogeneous reactions for asymmetric ring-opening of epoxides, oxidation, cyclopropanation, aziridination, reduction reaction of ketones, formation of cyclic and linear polycarbonates, epoxidation of olefins, catalytic enantioselective and diastereoselective redox reactions and Diels-Alder reactions.[10-13]

Research on oxidation of phenol in presence of clean oxidant such as H_2O_2 is of great importance due to its industrial applications. H_2O_2 with concentration of less than 60% is recognized as clean and green oxidizing agent amongst various oxidants.[14, 15] Products of phenol oxidation such as catechol and hydroquinone have many important applications as antioxidant, polymerization inhibitor, photographic film developer, flavoring agents, medicines and in organic synthesis etc.[16, 17]

Both catechol and hydroquinone are high demandable phenolic derivatives. These dihydroxybenzenes can be produced directly by hydroxylation of phenol in presence of environmentally benign oxidant, H_2O_2. The traditional catalysts used in this reaction are mineral acids,[18, 19] metal ions,[18, 20] and metal complexes.[21] However, these homogeneous catalysts have some drawbacks associated with their process of separation and recovery from the reaction mixture. Therefore, these drawbacks actually hinders their abundant uses in industry. Heterogeneous catalysis involving metal oxides and complexes always can impart alternate route and hence has been of keen interest for many researchers. In this perspective,

supported simple metal oxides,[22] complex metal oxides,[23, 24] zeolite-encapsulated metal complexes[25] and hydrotalcite-like compounds[26] are attractive catalysts for this reaction. Though, low catalytic activity and product selectivity have been noted for many of these catalysts and some of these catalysts follow complicated synthetic routes. Some of transition metal complexes, on the other hand, when encapsulated in the zeolites, have high catalytic activity, selectivity and their somewhat easy synthetic routes, low cost and high reaction rate actually trigger to utilize these encapsulated systems in the industry. Zeolite encapsulated metal complexes eventually have been used as target catalysts with the purpose of accelerating the rate of phenol hydroxylation reaction.

The study of the zeolite encapsulated metal complexes and their catalytic activities even has real significance because of their applications in variety of fields. Due to size and shape constraints provided by the zeolite walls, encapsulation approach can really improve the product selectivity and the lifetime of guest complex.[27] A metal complex once encapsulated in zeolites, encounters steric constraint imposed by topology of zeolite framework and also be in isolation from the other molecules of metal complex.[28] The molecular dimension of the guest metal complex once, is comparable with that of zeolitic cavities e.g., supercage in case of zeolite –Y , the complex may suffer from strong sterically constrained environment driven by the topology and architecture of zeolite-Y.[29] These steric and electrostatic environment actually control the geometry of the guest metal complex and consequently imply changes in magnetic, electronic and redox properties of the metal complex.[30] These modified properties thereby lead to change the catalytic activity of encapsulated metal complex. Subsequent possibility will be, the guest molecule inside the cage may show exciting properties that are not observed under free-state conditions. [31, 32]

Syntheses of transition metal Schiff-base complexes inside the supercage of zeolite have achieved attention considerably because of their exciting contribution in catalysis. Zeolite encapsulated metal complexes reported till now primarily find their applications in heterogeneous catalysis[33-35] like shape-selective epoxidation of alkenes[36], oxidation of styrene and cyclohexene[37] and phenol oxidation[38].

To investigate the effect of structural modifications of the zeolite encapsulated Ni(II) salophen complexes on their catalytic activity, an effort has been made to synthesize zeolite encapsulated Ni(II) Schiff-base complexes with two different series of salophen ligand (sal-1,2-phen and sal-1,3-phen) having H, -OCH_3, -NO_2 substituent groups, as shown in Figure 6.1. This chapter hence, discusses the syntheses of zeolite encapsulated Ni(II)

Schiff-base complexes and their reactivity towards hydroxylation of phenol. In the current study, in addition to the syntheses, detailed characterization and reactivity have been scrutinized for the encapsulated nickel salophen complexes. The current chapter focuses on the structural modification studies of these nickel complexes under encapsulation since the structural modification triggers significant changes in their electronic, magnetic and catalytic activities. Comparative structural and catalytic studies of two series of Schiff-base complex series are under consideration currently with the purpose of observing the effect of site isolation as well. Comparative studies impart quite a fascinating understanding about the catalysis of these host-guest systems along with the modified electronic structure of the encapsulated complexes which subsequently leaves a lot of opportunities to further tune the catalytic activity of the catalysts.

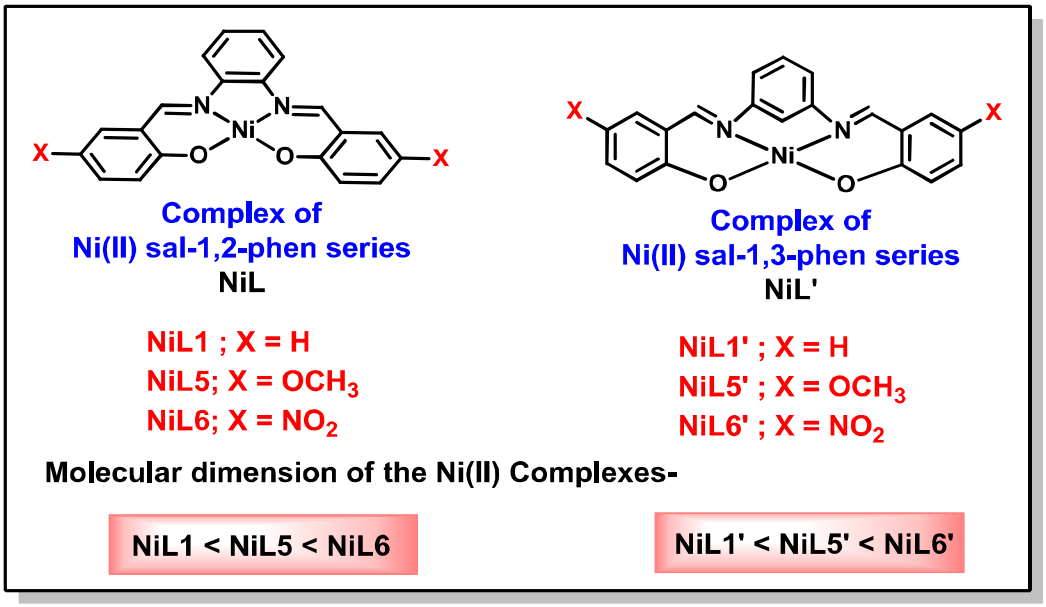

Figure 6.1: Schematic representation of Nickel Schiff-base complexes.

6.2 RESULTS AND DISCUSSION

Synthesis of ligands and nickel Schiff-base complexes in free or encapsulated states have already been discussed in chapter 2 under experimental section (2.2.1-2.2.5).

6.2.1 Elemental Analysis

Energy dispersive X-ray spectroscopy (EDX) technique confirms the presence of the different elements in the encapsulated nickel systems and Ni(II) exchanged zeolite Y along with their weight% (data provided in Table 6.1). Elemental analysis indicates the Si to Al weight% ratio of parent zeolite-Y as 2.7 corresponding to the unit cell formula as $Na_{52}(AlO_2)_{52}(SiO_2)_{140}$. yH_2O. The Si/Al ratio has changed marginally during metal exchange reaction and encapsulation process, which indeed confirms the nominal dealumination during the whole process of encapsulation. The amount of nickel metal in all Soxhlet extracted encapsulated systems is found to be less as compared to that in Ni(II) exchanged zeolite -Y. The reduction in the nickel concentration during the formation of complex inside the supercage of zeolite Y is an indirect evidence of complex formation inside. This observation therefore, proves that Soxhlet extraction has successfully removed the complexes that are formed on the surface, leading into the overall reduction of Ni content as compared to the parent Ni-exchanged zeolite.

Table 6.1: Concentration of nickel (wt %) content in the different Samples.

S.No.	Samples	Nickel (wt%)	Si/ Al ratio
1	**Zeolite-Y**	-	2.79
2	**Ni-Y**	2.13	2.79
3	**NiL1-Y**	0.52	2.78
4	**NiL5-Y**	0.54	2.79
5	**NiL6-Y**	0.45	2.78
6	**NiL1′-Y**	0.55	2.79
7	**NiL5′-Y**	0.56	2.78
8	**NiL6′-Y**	0.42	2.79

6.2.2 X-Ray Diffraction (XRD) studies

To prove crystallinity and integrity of zeolite framework after encapsulation processes, we have performed powder X-ray diffraction (PXRD) analysis for zeolite-NaY, Ni(II) exchanged zeolite-NaY and all zeolite samples having encapsulated Ni(II) complexes (XRD patterns presented in Figure 6.2). Nearly identical

XRD patterns certainly confirm the retention of crystalline structure of zeolite during the process of encapsulation of Ni(II) Schiff-base complexes.[39] Only difference is apparent in the intensities of the diffractions at (220) and (311) planes appearing at 2θ of 10° and 12° respectively. The initial intensity relationship of $I_{220} > I_{311}$ observed for the parent zeolite-Y and Ni(II) exchanged zeolite-Y goes for intensity reversal as $I_{220} < I_{311}$ for the all encapsulated systems. Such observations already has been notified and empirically correlated only with the presence of large molecule inside the supercage of zeolite-Y.[31, 32, 40-42] It is never observed when complex formation takes place on the surface of the host framework.[32] Thereby, the successful encapsulation of Ni(II) Schiff-base complexes inside the cavity of host framework is proven consequentially.

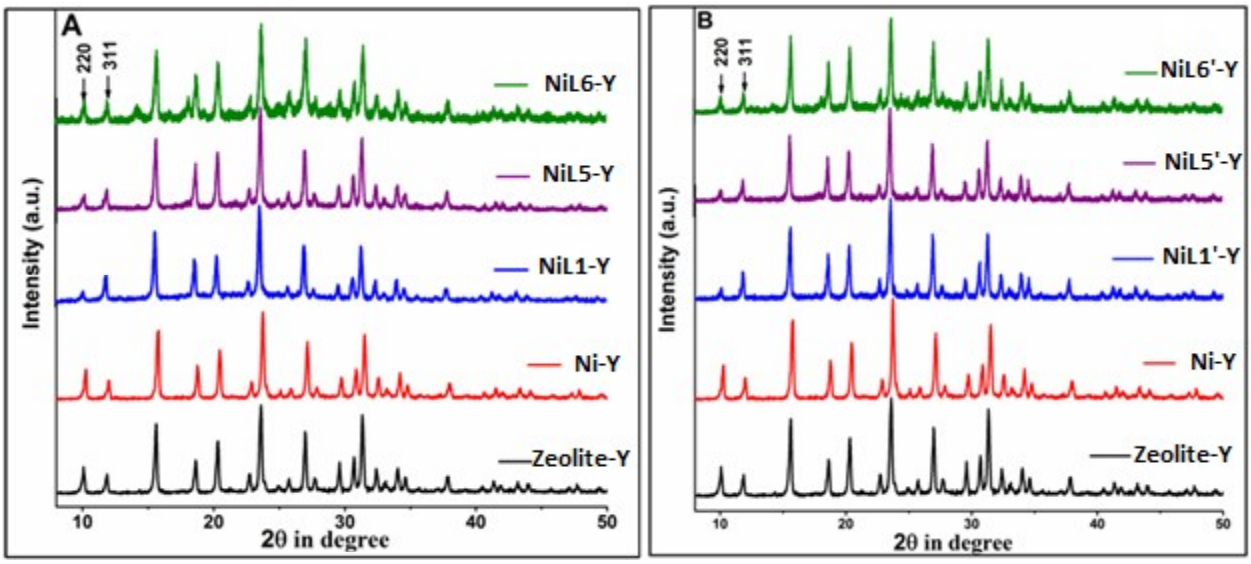

Figure 6.2: (A) XRD patterns of pure zeolite-Y, Ni-exchanged zeolite -Y, NiL1-Y, NiL5-Y and NiL6-Y and (B) XRD patterns of pure zeolite-Y, Ni-exchanged zeolite -Y, NiL1′-Y, NiL5′-Y and NiL6′-Y.

6.2.3 Scanning Electron Microscopy (SEM)

The Ni(II) Schiff-base complexes have been synthesized inside the supercage of zeolite Y by using 'flexible ligand method'. However, target synthesis of complex only inside the supercage is practically not viable as some of these complex molecules definitely get synthesized on the host framework or some

ligand molecules may remain unreacted. Therefore, Soxhlet extraction becomes mandatory till the solvent becomes colourless to remove the uncoordinated ligand molecules and complexes adsorbed on surface of the host framework. The surface morphology of the host framework is studied by scanning electron micrographs for all these zeolite samples before and after Soxhlet extraction (SE micrographs of zeolite with encapsulated NiL1 complex presented in Figure 6.3). Before Soxhlet extraction, surface adsorbed species are clearly visible on host framework, however are entirely removed after the extraction. Thereby, boundaries of the zeolite particles are clearly evident for Soxhlet extracted samples and the final pale color of the encapsulated complex is an indication for the encapsulation of metal complex inside the cavity of host.

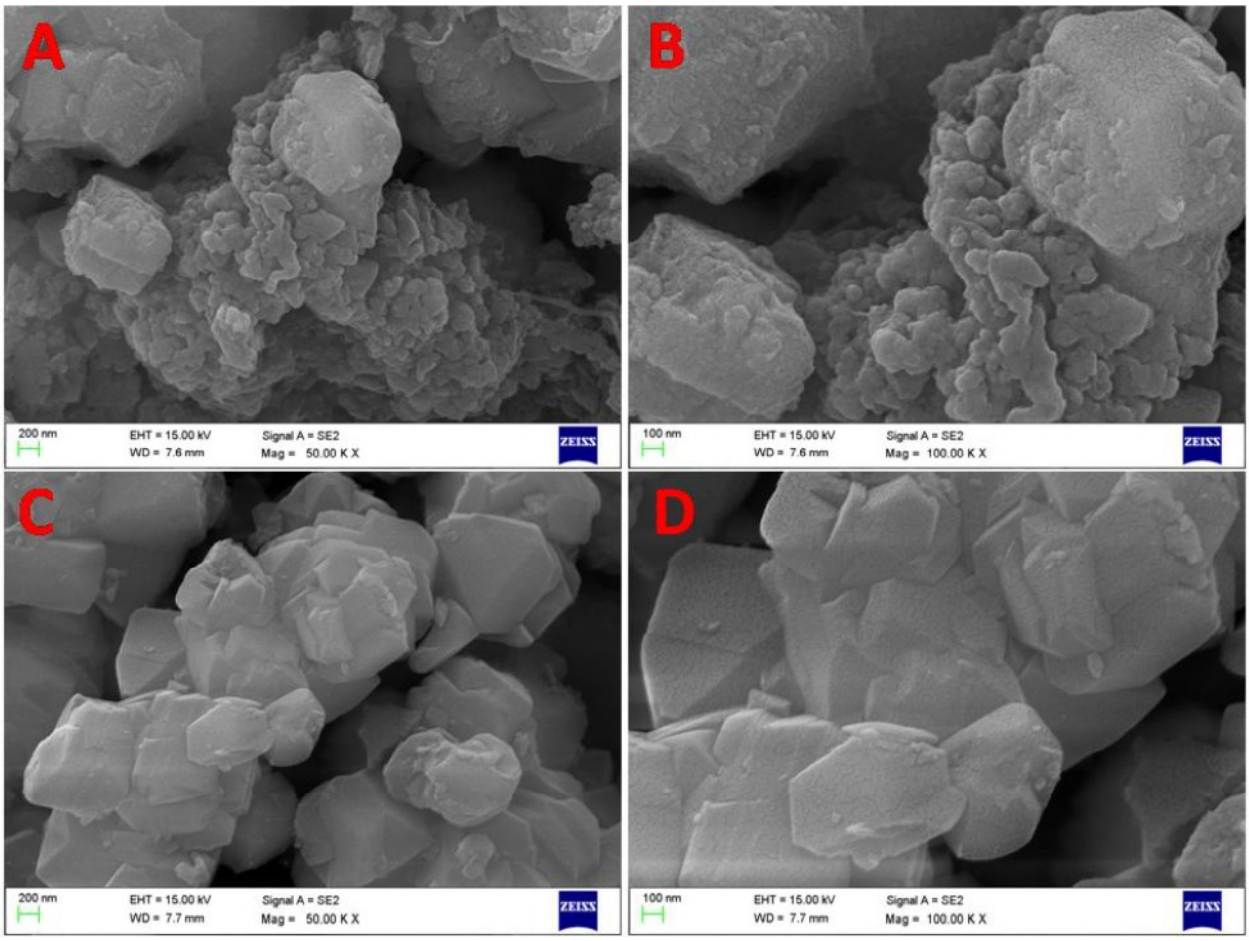

Figure 6.3: SE micrograph of the encapsulated NiL1 in zeolite Y, (A) and (B) (before Soxhlet extraction), (C) and (D) (after Soxhlet extraction).

6.2.4 BET surface area analysis

N_2 adsorption-desorption isotherms obtained from BET surface area analysis of the pure zeolite-Y and encapsulated Ni(II) Schiff-base complexes (presented in Figure 6.4 and Table 6.2 for NiL1-Y and NiL1′-Y) show typically type I isotherm indicating the microporous nature of the samples.[43, 44] An interesting observation is noticed in the comparative study of the surface area and pore volume of parent zeolite-Y and encapsulated systems. Significant lowering in BET surface area and pore volume of pure zeolite-Y after undergoing the process of encapsulation certainly suggest that Ni(II) Schiff-base complex is present inside the inner space of zeolite i.e., supercage rather than on the surface.[31, 45] The reduction in the BET surface area and pore volume of zeolite-Y during encapsulation depends on the loading level of metal along with the molecular dimension of the complex inside the cavities of zeolite framework.

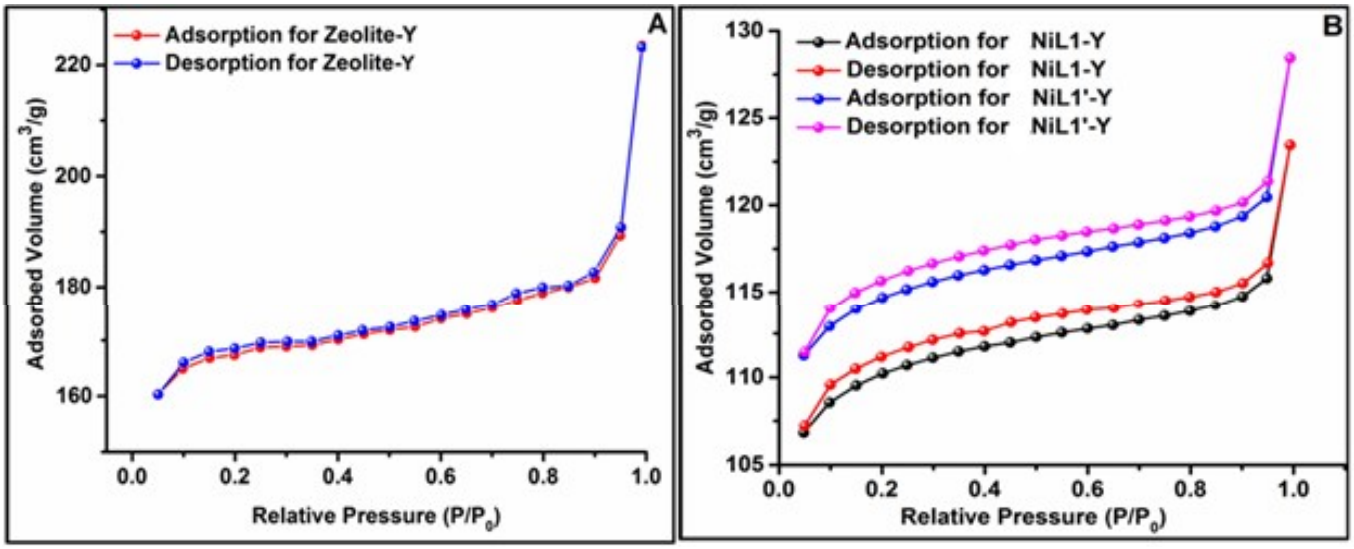

Figure 6.4: BET isotherms for pure zeolite-Y and zeolite encapsulated complexes: (A) pure zeolite-Y, (B) NiL1-Yand NiL1′-Y.

Table 6.2: BET surface area and pore volume of pure zeolite Y and encapsulated nickel complexes (NiL1-Y and NiL1′-Y).

S.No.	Sample	BET surface area (m^2/g)	Pore volume (cm^3/g)
1	**Pure zeolite Y**	535	0.3456
2	**NiL1-Y**	320	0.1904
3	**NiL1′-Y**	328	0.2106

6.2.5 Thermal analysis

To determine the thermal stability of neat and encapsulated Ni(II) Schiff-base complexes thermo-gravimetric (TGA) analysis has been done in the temperature range of (25 – 800)°C under inert atmosphere with a heating rate of 10 °C/minute (The TGA plots of zeolite -Y, free state and encapsulated nickel complexes presented in Figure 6.5. The neat complexes show weight loss only due to decomposition of ligand moiety whereas all encapsulated nickel complexes show an additional weight loss in the temperature range of (30 – 185) °C due to loss of intrazeolite water molecules. The second step of weight loss widens in the temperature range of (300 – 780) °C suggesting slow decomposition of coordinated ligand and is of relatively lesser extent in comparison to the corresponding free-state nickel complexes. These results indicate the presence of low loading level of nickel complex inside the supercage of zeolite Y and well in agreement with the results obtained by the EDX analysis. Encapsulated systems show the decomposition temperature extends towards higher temperature, which is the indication of thermal stability of the encapsulated nickel complexes.

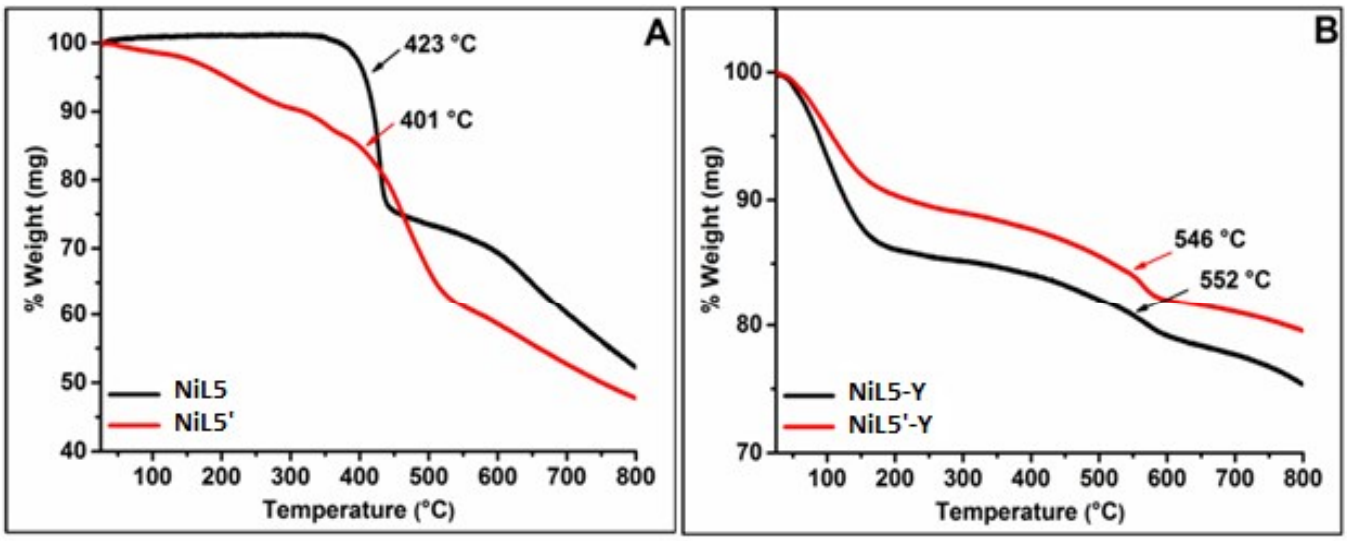

Figure 6.5: Thermogravimetric analysis (TGA) results for (A) NiL5 and NiL5′ free state complex and (B) NiL5-Y and NiL5′-Y encapsulated complex.

6.2.6 Fourier Transform Infrared spectroscopy (FTIR)

Figure 6.6 represents the FTIR data of parent zeolite-Y and encapsulated nickel Schiff-base complexes. The IR bands of pure zeolite-Y are mainly present below 1200 cm^{-1}. IR spectra of parent zeolite Y (Figure 6.6) exhibit strong IR bands in the range 500−1200 cm^{-1}. The strong FTIR band at the region 1010−1040 cm^{-1} are obtained due to the asymmetric stretching vibrations of (Si/Al) O_4 units of zeolite host framework. The noticeable broad bands at 1643 and 3500 cm^{-1} are attributed to lattice water molecules and surface hydroxylic groups, respectively. Some of characteristic peaks at 560, 717, and 786 cm^{-1} (Figure 6.6) are assigned as T−O bending mode, double ring and symmetric stretching vibrations respectively. These FTIR bands are not altered upon encapsulation process (Figure 6.6). Zeolite framework retains its integrity during encapsulation of nickel Schiff base complexes which is proved by the IR bands of parent zeolite Y remain unchanged during metal exchange reaction and encapsulation process. However, a significant difference is observed in the range of 1200−1600 cm^{-1} for the encapsulated system (see Figure 6.6). Parent zeolite-Y does not show any absorption band in this region, so it is appropriate region for the study of encapsulated M(II) Schiff-base complexes. In this region, FTIR bands are found in the range of 1200−1600 cm^{-1} only because of the metal complexes. The FTIR peaks

of encapsulated nickel Schiff-base complexes are very weak due to their low concentration in the zeolite framework. The important FTIR peaks are summarized in Table 6.3 for both free-state and encapsulated nickel complexes.

Due to the C=N and C-O stretching vibrations in the Schiff-base ligands, IR peaks are observed at 1612-1620 cm^{-1} and 1273-1296 cm^{-1}which are slightly shifted towards lower frequency after complexation, indicates that nitrogen and oxygen are taking part in the coordination. FTIR spectra of free-state nickel complex show two strong bands at 1593-1609 cm^{-1} and 1257-1296 cm^{-1} are due to C=N and C-O stretching vibrations. The FTIR bands at 1444-1539 cm^{-1} corresponds to C=C stretching and band at 1373-1396 cm^{-1} assigned to ν_{C-H} deformation. The FTIR bands have very less intensity in case of encapsulated system. Characteristic feature further indicates the absence of extraneous nickel complex on the surface of zeolite-Y. The presence of similar IR bands in the free-state and encapsulated metal complexes provides the indirect proof for the presence of a Ni(II) Schiff base complex within the super cage of zeolite-Y. The slight shifting in the FTIR band positions can be attributed due to the effect of zeolite framework on the geometry of the metal complexes entrapped in the cavities of zeolite-Y. The slight shift in ν_{C-H} deformation band after encapsulation of metal complex reveals the sign for the encapsulation of nickel complex inside the supercage of zeolite Y.

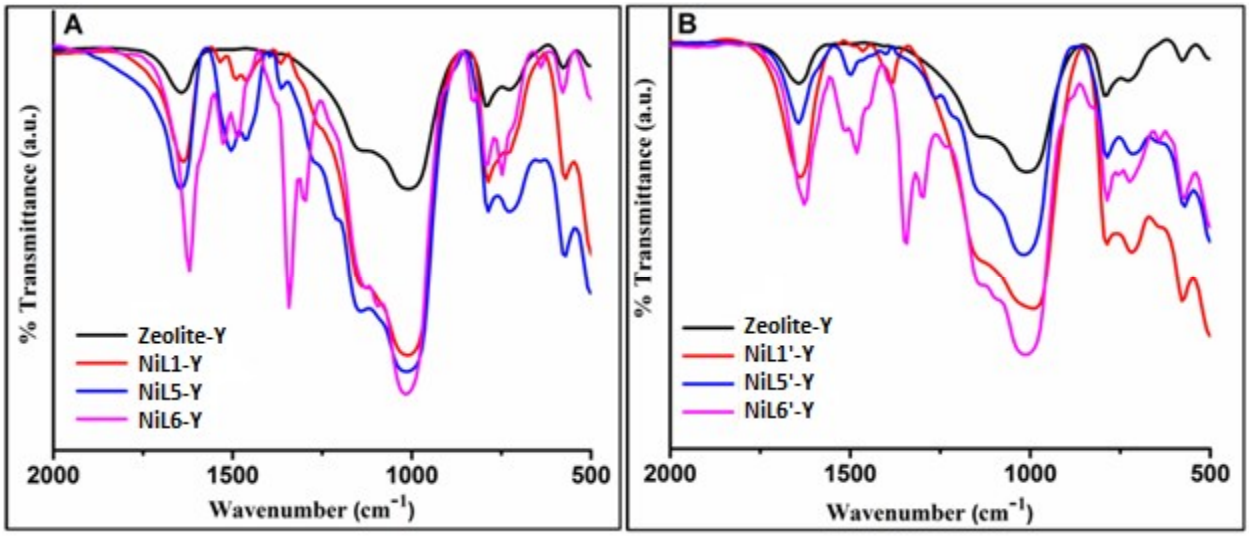

Figure 6.6: FTIR spectra of (A) pure zeolite-Y, NiL1-Y, NiL5-Y and NiL6-Y and (B) pure zeolite-Y, NiL1′-Y, NiL5′-Y and NiL6′-Y.

Table 6.3: FTIR data of neat and encapsulated complexes.

S. No	Samples	C=N stretching	C=C stretching	C-H deformation	C-O stretching
1	**NiL1**	1605	1520, 1443	1381	1296
2	**NiL1-Y**	1636	1489, 1458	1396	1292
3	**NiL5**	1605	1528, 1466	1381	1277
4	**NiL5-Y**	1643	1504, 1458	1396	1265
5	**NiL6**	1612	1543, 1481	1381	1257
6	**NiL6-Y**	1620	1528, 1489	1389	1254
7	**NiL1′**	1589	1543, 1466	1389	1250
8	**NiL1′-Y**	1643	1489, 1458	1358	1292
9	**NiL5′**	1589	1516, 1474	1381	1273
10	**NiL5′-Y**	1643	1497, 1442	1396	1265
11	**NiL6′**	1612	1528, 1482	1372	1256
12	**NiL6′-Y**	1628	1520, 1481	1342	1296

6.2.7 X-ray Photoelectron Spectroscopy (XPS)

The X-ray Photoelectron Spectroscopy (XPS) analysis for free state (NiL1 and NiL1′) and encapsulated nickel complexes (NiL1-Y, NiL5-Y, NiL1′-Y and NiL5′-Y) furnishes the relative concentration of elements and their chemical states in the samples. It indicates the presence of C, N, O and Ni(II) in their relevant chemical states in all the complexes and also Si, Al and Na in the encapsulated systems. XPS spectra are shown in Figure 6.7-6.13. From the comparison of XPS signal intensity of Ni 2p level, the fact emerged is that the encapsulated systems have quite a low concentration of nickel ions than the free state complexes which is just in line with the EDX, FTIR and UV-Vis results. Survey spectra of the nickel

complexes presented in Figure 6.7, indicates the presence of Ni, C, N and O in free as well as in encapsulated states.

The presence of Ni^{+2} is confirmed by the $Ni2p_{3/2}$ and $Ni2p_{1/2}$ peaks appearing at binding energies of 856.24 and 873.59 eV, respectively, for NiL1. The observed binding energy for Ni(II) is lower than the usually Ni(II) holding octahedral geometry and moreover, the absence of any shakeup satellite peak beyond 878 eV confirms the square planar geometry of nickel complex.[38] However a distinct difference exists in the deconvoluted spectra of Ni2p of NiL1 and NiL1′ complexes. The $2p_{3/2}$ and $2p_{1/2}$ peaks of Ni(II) in NiL1′ are observed at the binding energies of 856.24 and 873.77 eV, respectively, along with two shakeup satellite broad peaks at the binding energies of 861.63 and 879.70 eV, respectively. This indicates the disturbed environment of the square planar geometry around the metal center and is in agreement with our previously reported theoretical results.[46]

In case of encapsulated system NiL1-Y, the $2p_{3/2}$ and $2p_{1/2}$ peaks of Ni(II) appear at the binding energies of 856.24 and 873.42 eV, respectively. Two shakeup satellite peaks at the binding energies of 862.35 and 882.07 eV are the indicatives of the change in the coordination geometry of Ni(II) in the entrapped form. Encapsulated NiL1′-Y system does not recommend any significant change of its geometry under encapsulation.

The C(1s) XPS peaks are broad and intense for all the complexes, which is further deconvoluted into two peaks at the binding energies of 285.41 and 287.02 eV, confirming the presence of two different type of carbon atoms (sp^3 and sp^2 types) in the samples. The O(1s) and N(1s) XPS traces are also found at the expected binding energies according to literature.[31, 47] For encapsulated system NiL1-Y, the Si(2p), Al(2p) and Na(1s) appear at the binding energies of 103.27, 74.93 and 1072.85 eV respectively. All the encapsulated systems like NiL5-Y and NiL1′-Y show the same type of XPS spectra with the presence of Si(2p), Al(2p) and Na(1s) signals. The presence of $Ni2p_{3/2}$, $Ni2p_{1/2}$, C(1s), N(1s), O(1s), Si(2p), Al(2p) and Na(1s) XPS signals for the encapsulated nickel complexes are just in accordance with the signals observed for free state nickel complexes (presented in Table 6.4) demonstrating the formation of the complex within the supercage of zeolite Y.

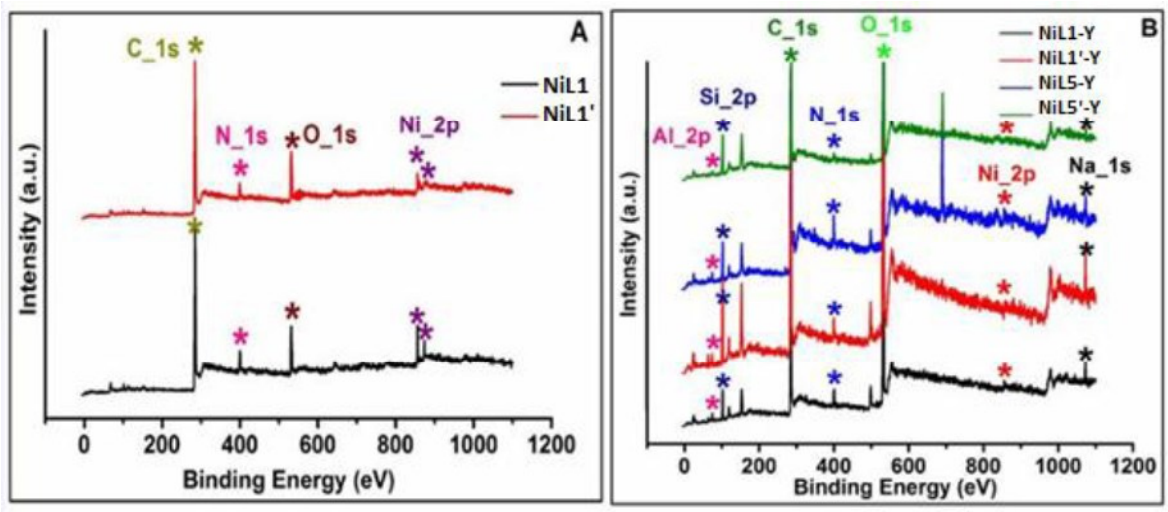

Figure 6.7: XPS survey spectra of (A) neat complexes NiL1 and NiL1′ (B) encapsulated complexes NiL1-Y, NiL1′-Y, NiL5-Y and NiL5′-Y.

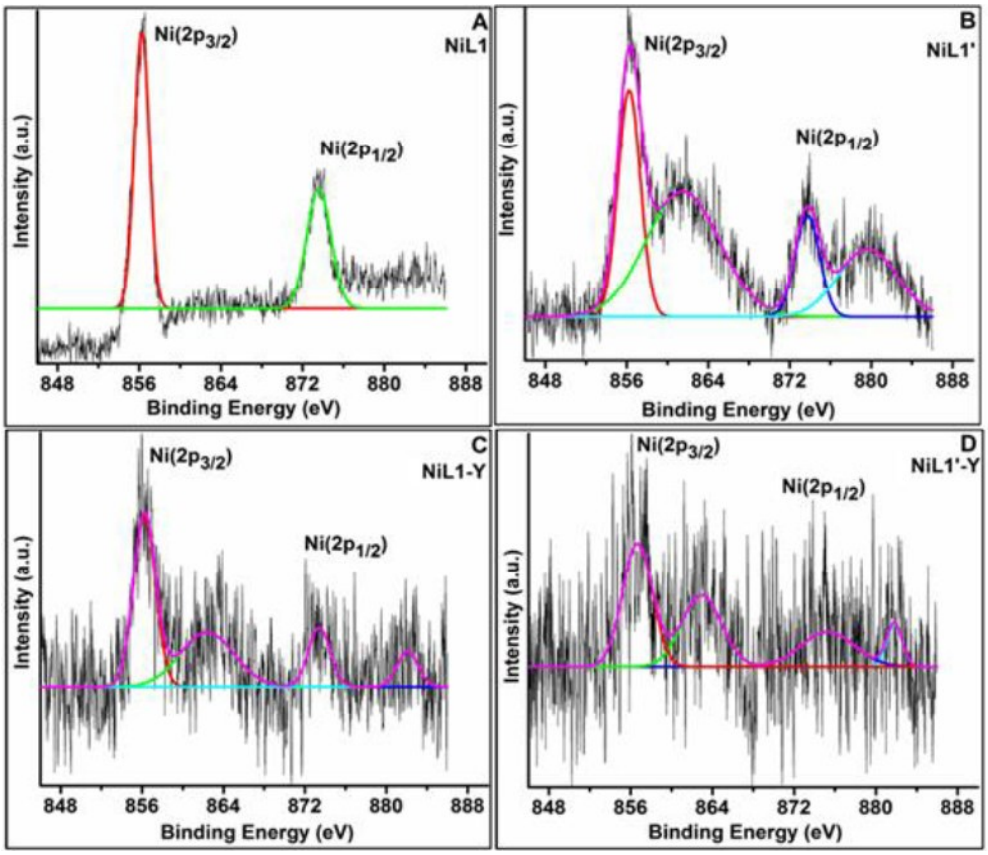

Figure 6.8: High resolution XPS signals of Ni (2p) for (A) NiL1, (B) NiL1′, (C) NiL1-Y and (D) NiL1′-Y complex.

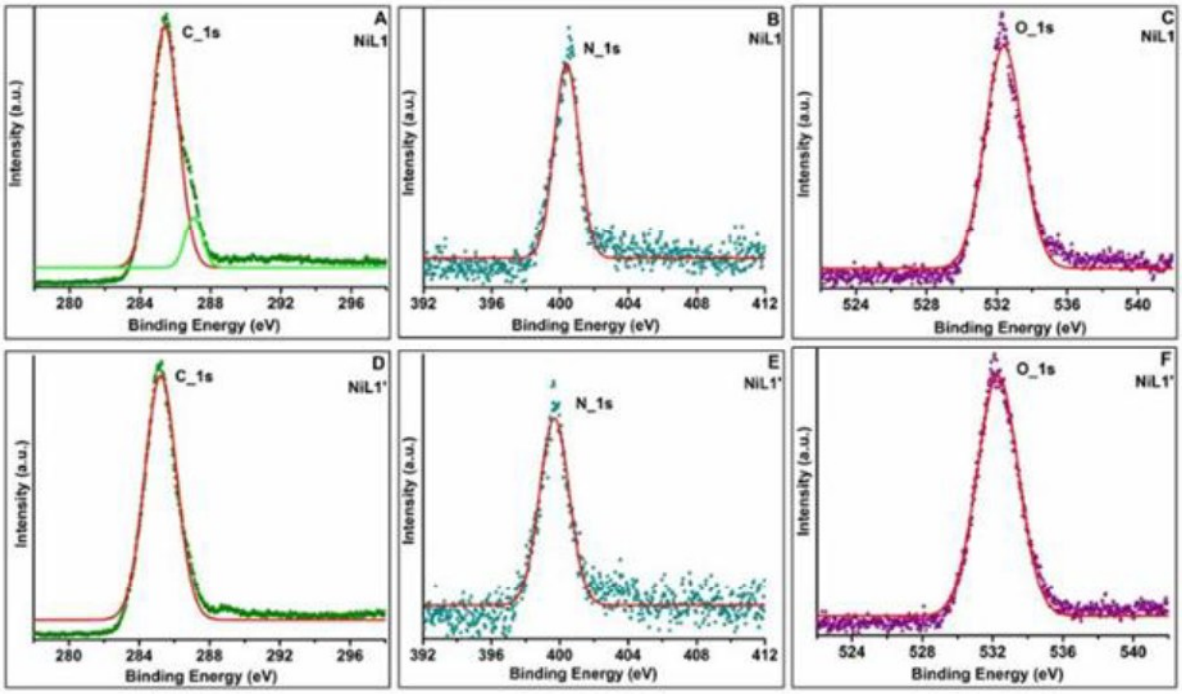

Figure 6.9: High-resolution XPS spectra of C (1s), N (1s), and O (1s) for NiL1 and NiL1′ complex.

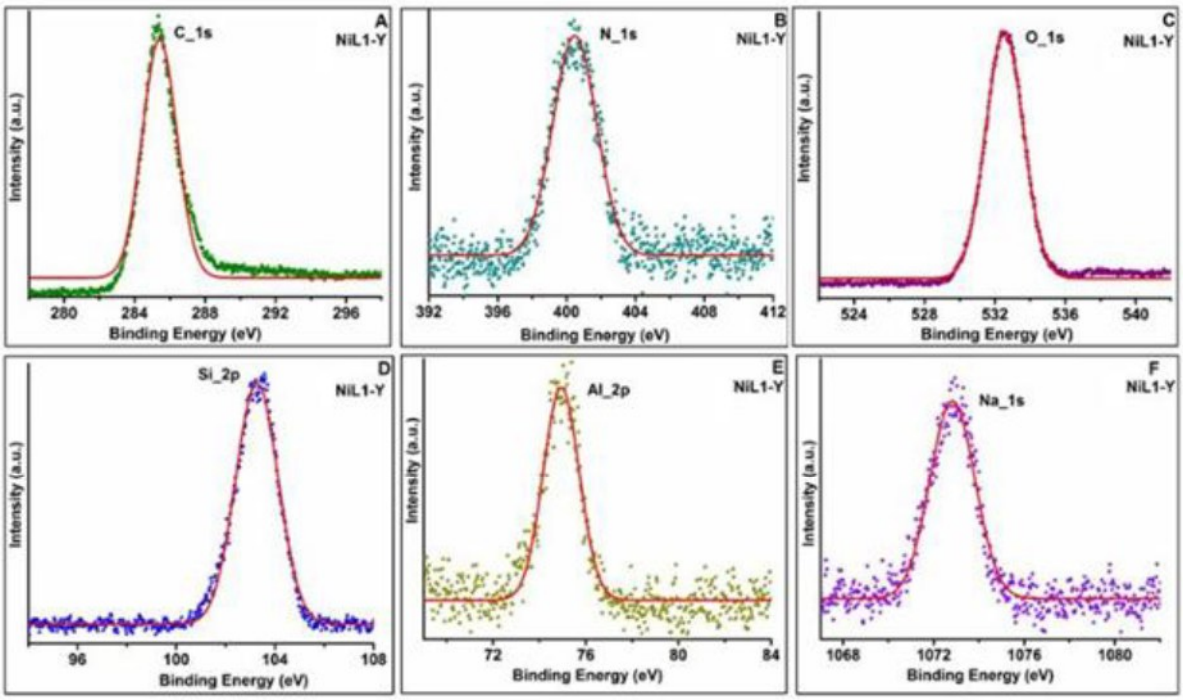

Figure 6.10: High-resolution XPS spectra of C (1s), N (1s), O (1s), Si (2p), Al (2p) and Na (1s) for NiL1-Y complex.

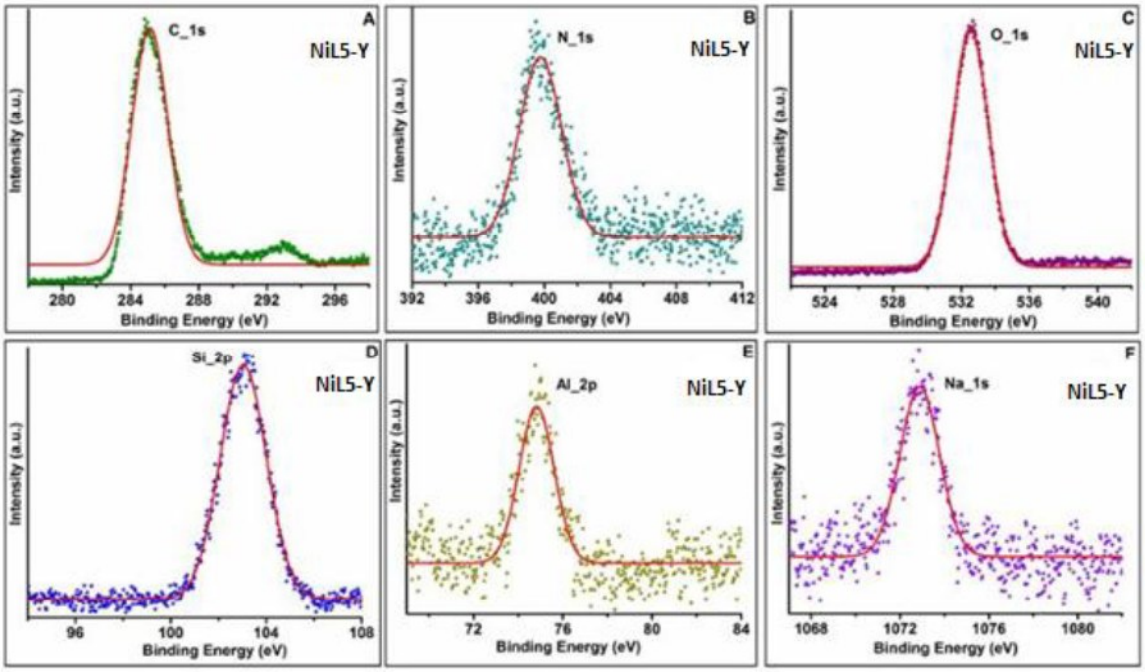

Figure 6.11: High-resolution XPS spectra of C (1s), N (1s), O (1s), Si (2p), Al (2p) and Na (1s) for NiL5-Y complex.

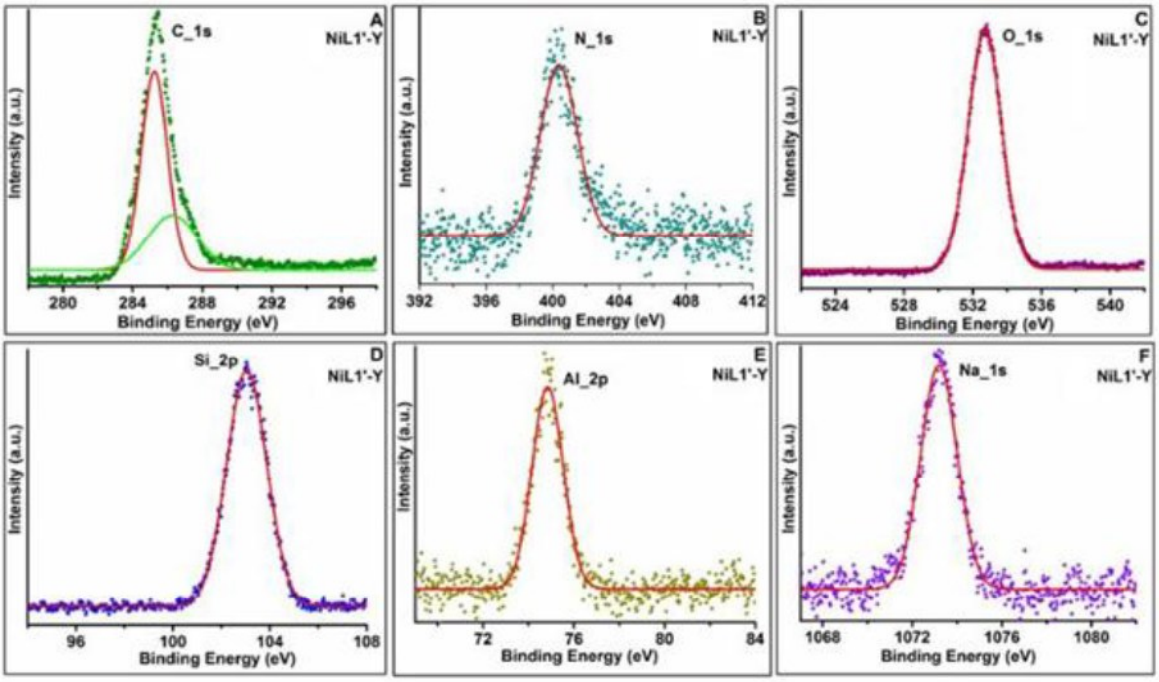

Figure 6.12: High-resolution XPS spectra of C (1s), N (1s), O (1s), Si (2p), Al (2p) and Na (1s) for NiL1′-Y complex.

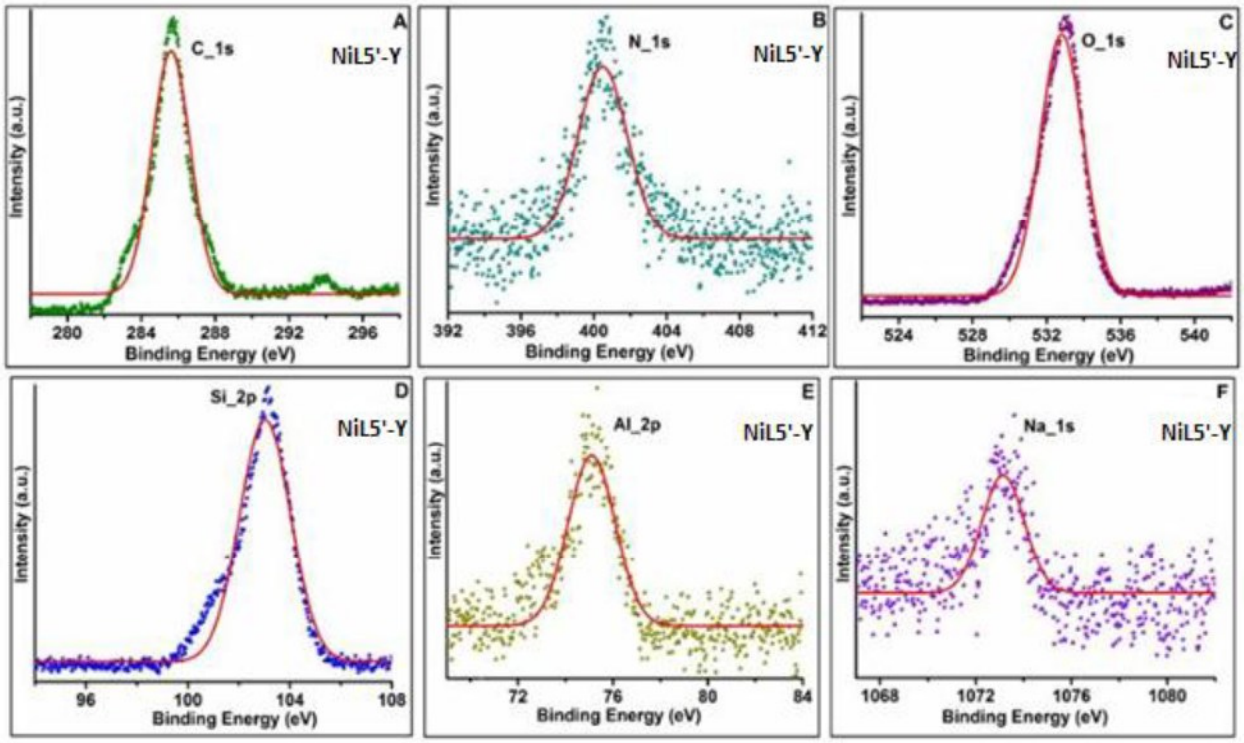

Figure 6.13: High-resolution XPS spectra of C (1s), N (1s), O (1s), Si (2p), Al (2p) and Na (1s) for NiL5′-Y complex.

Table 6.4: Binding energy (eV) of neat and encapsulated complexes.

S. No	Samples	Si (2p)	Al (2p)	Na (1s)	C (1s)	N(1s)	O (1s)	Ni ($2p_{3/2}$)	Ni ($2p_{1/2}$)
1.	**NiL1**	-	-	-	285.41, 287.02	400.38	532.37	856.24	873.59
2.	**NiL1′**	-	-	-	285.22, 287.08	399.69	532.29	856.24, 861.63	873.77, 879.70
3.	**NiL1-Y**	103.27	74.93	1072.85	285.41, 287.20	400.46	532.52	856.24, 862.35	873.42, 882.07
4.	**NiL5-Y**	103.05	74.82	1072.91	285.14, 287.20	399.80	532.56	855.22, 861.28	873.07, 881.55
5.	**NiL1′-Y**	103.28	74.90	1072.84	285.36, 287.22	400.44	532.51	856.67, 863.00	875.31, 881.75
6.	**NiL5′-Y**	103.04	74.88	1072.78	285.38, 287.06	399.24	532.54	855.21, 861.26	872.95, 881.35

6.2.8 UV-Vis/Diffuse Reflectance Spectroscopy (UV−Vis/ DRS)

The electronic spectroscopic studies always remain very informative to comprehend the geometry and reactivity of such host-guest systems. The electronic spectra of the Schiff-base ligands and free state Ni(II) complexes are recorded in $CHCl_3$ (shown in Figure 6.14 with summary of data presented in Table 6.5). The nickel salophen complex (NiL1) shows four intense bands. The bands at 260, 294 and 379 nm are assigned as intra-ligand π-π^* transition and n-π^* transitions. However, the absorption band at 483 nm is either charge transfer or d-d transitions involving the metal center which strongly supports the complex formation as this band is absent in the spectrum of the corresponding ligand (L1).

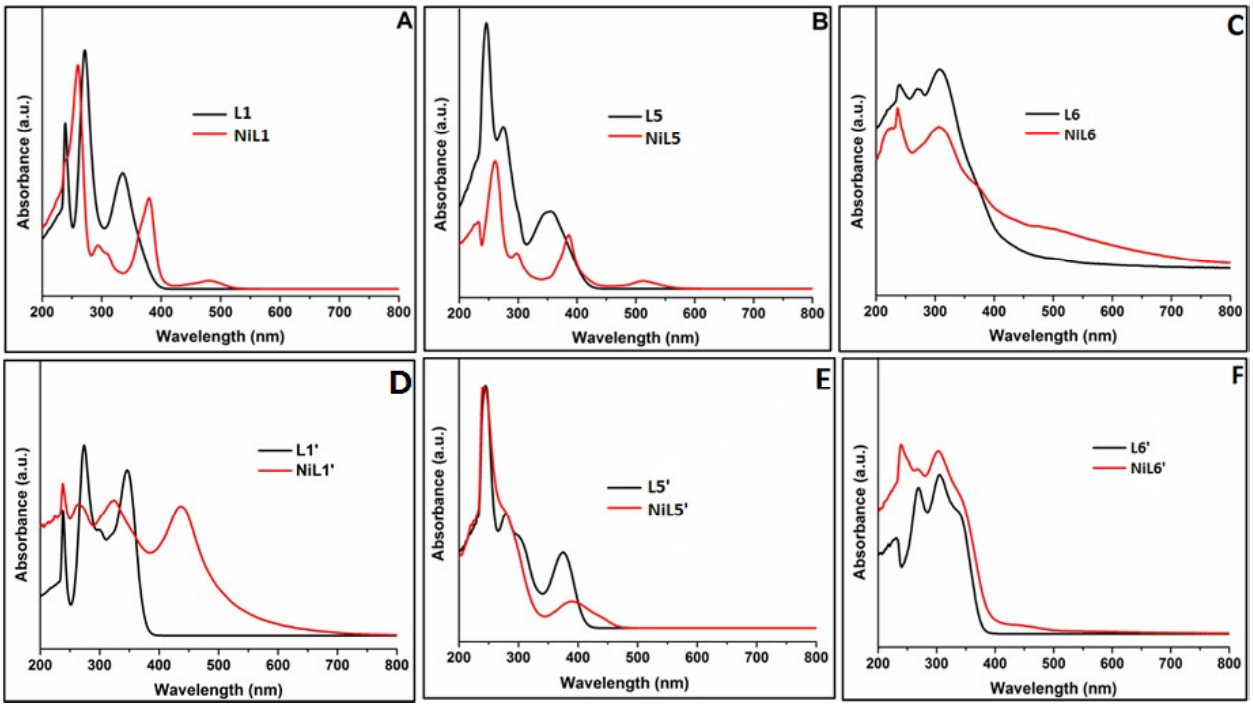

Figure 6.14: Solution UV-Vis spectra of (A) L1 and NiL1, (B) L5 and NiL5 and (C) L6 and NiL6, (D) L1′ and NiL1′, (E) L5′ and NiL5′ and (F) L6′ and NiL6′.

Table 6.5: Solution UV-Visible data of ligand and neat complexes.

S. No	Samples	π—π^* transitions	n—π^* transitions	CT transitions / d-d transitions
1	**L1**	272, 283	335, 364	-
2	**NiL1**	260, 294	360, 379	483
3	**L5**	246, 275	350, 378	-
4	**NiL5**	260, 298	365, 385	514
5	**L6**	240, 271	308, 364	-
6	**NiL6**	246, 274	310, 372	480
7	**L1′**	273, 298	345	
8	**NiL1′**	276, 302	323, 350	437
9	**L5′**	244, 279	302, 375	
10	**NiL5′**	245, 281	301, 380	443
11	**L6′**	268	305, 338	
12	**NiL6′**	269	302, 343	432

The DRS / solid state UV−Vis spectra and spectral data of free state and encapsulated Ni(II) Schiff-base complexes are presented in Figure 6.15 and Table 6.6. The transition originated from the metal of NiL5 complex is red shifted and that of NiL6 is blue shifted as compared to those of NiL1 complex. This is well understood as NiL5 complex has strong electron donating groups (-OCH_3 groups) and NiL6 is having strong electron withdrawing groups (-NO_2 groups) in the ligand moiety. Another interesting observation is that the lowest energy transition, indeed originated from the metal of NiL1 is found to be red shifted in comparison to that of NiL1′ complex directing to the fact that L series of ligands provide more electron density around the metal as compared to L′ series.

The comparison of the UV-Vis study of the free state NiL1 complex with those of the encapsulated NiL1-Y complex unfolds the blue shift of the lowest energy band originated from the metal upon encapsulation

whereas the sane transition is red shifted in case of NiL1′-Y complex. Encapsulation, enforces metal related transition for all L series complexes to undergo blue shifts however, all L′ series of Ni(II) complexes are showing red shift. This phenomenon is undoubtedly the consequence of geometrical modification of metal complexes after encapsulation and is pointing towards the fact that L and L' series promote two different and nearly opposing kinds of structural modifications. Red shift in metal related transition for encapsulated Ni(II) Schiff-base complexes suggests enhanced π-delocalization around the metal and blue shifts indicate the interrupted π-delocalization.

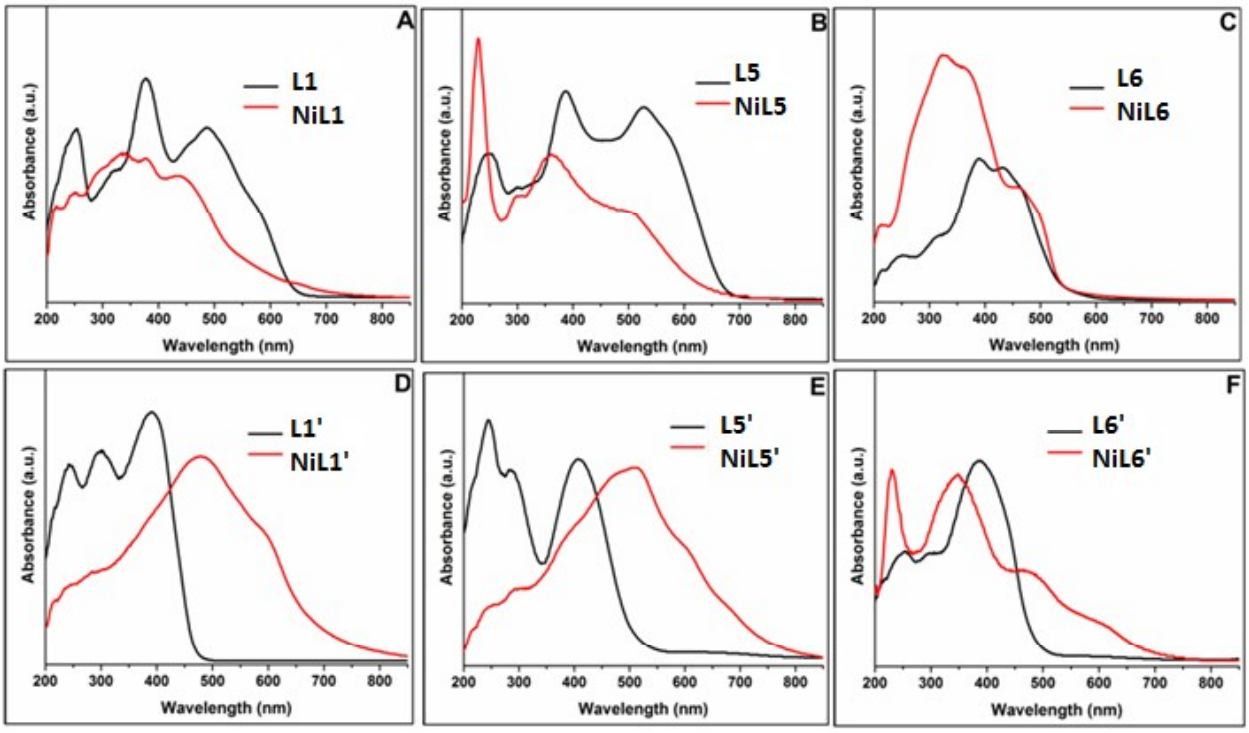

Figure 6.15. Solid state UV-Vis spectra of (A) NiL1 and NiL1-Y, (B) NiL5 and NiL5-Y, (C) NiL6 and NiL6-Y, (D) NiL1′ and NiL1′-Y, (E) NiL5′ and NiL5′-Y and (F) NiL6′ and NiL6′-Y.

Table 6.6: Solid-state UV-Visible data of neat and encapsulated complexes.

S. No	Samples	π—π^* transitions	n—π^* transitions	CT transitions / d-d transitions
1	**NiL1**	255	320, 378	487, 580
2	**NiL1-Y**	252	335, 380	448, 556
3	**NiL5**	250	298, 386	526, 578
4	**NiL5-Y**	230	302, 362	509, 580
5	**NiL6**	250	316, 386	439, 469
6	**NiL6-Y**	260	322, 372	464, 496
7	**NiL1′**	243	298, 387	440
8	**NiL1′-Y**	245	284, 380	474, 596
9	**NiL5′**	243	285,	407, 468
10	**NiL5′-Y**	248	294, 392	515, 608
11	**NiL6′**	254	297, 386	445
12	**NiL6′-Y**	232	349	480, 615

6.2.9 Magnetic Study

To know the effect of host framework specifically on the geometry of guest complex, magnetic measurements have been carried out for the Ni(II) complexes in both their neat and encapsulated states by using a SQUID magnetometer. The molar susceptibility (χ_M) vs. temperature (T) K for both the neat and encapsulated states are presented in Figure 6.16. In neat state, the Ni(II) in NiL1 and NiL1′ are diamagnetic in nature and magnetic moment appears to be close to zero (ranging from 0.43–0.46μ_B). The nature of molar susceptibility (χ_M) vs. temperature (T) K (shown Figure 6.16A) confirms diamagnetic behavior of NiL1 manifesting planarity around the Ni(II) center. However, the case is different for NiL1′ complex as it exhibits paramagnetism to certain extent. These results are in agreement with the XPS observations and

previously reported theoretical studies as well,[46] which once again identifies NiL1′ complex with devoid of planarity to a greater extent as compared to NiL1 system.

Encapsulated Ni(II) Schiff-base complexes are demonstrating improved magnetization that is certainly from the guest complexes as zeolite host is diamagnetic in nature.[48, 49] The most plausible reason could be the distortion that these salophen complexes undergo upon encapsulation in order to be accommodated inside the supercage. These geometric modifications subsequently, reshuffles the ordering of molecular energy levels and thereby alters the electronic environment around the metal center.

All the encapsulated systems show an enhanced magnetism and encapsulated complexes of L′ series exhibit higher magnetization than that of the encapsulated nickel complexes of L series probably because of the geometry of the complexes in L′ series is fundamentally non-planar in their free states. With increase of molecular dimension, the extent of non-planarity increases on encapsulation and thereby the magnetization. Both the series exhibit the very similar trend of enhancement of magnetization along with the increasing order of molecular dimension of the complexes. Magnetism is maximum for NiL6′-Y than NiL5′-Y and then is for NiL1′-Y complex. Zeolite encapsulated NiL6′-Y complex shows the highest magnetic moment among all the encapsulated Ni(II) Schiff-base complexes (2.85μ_B at room temperature).

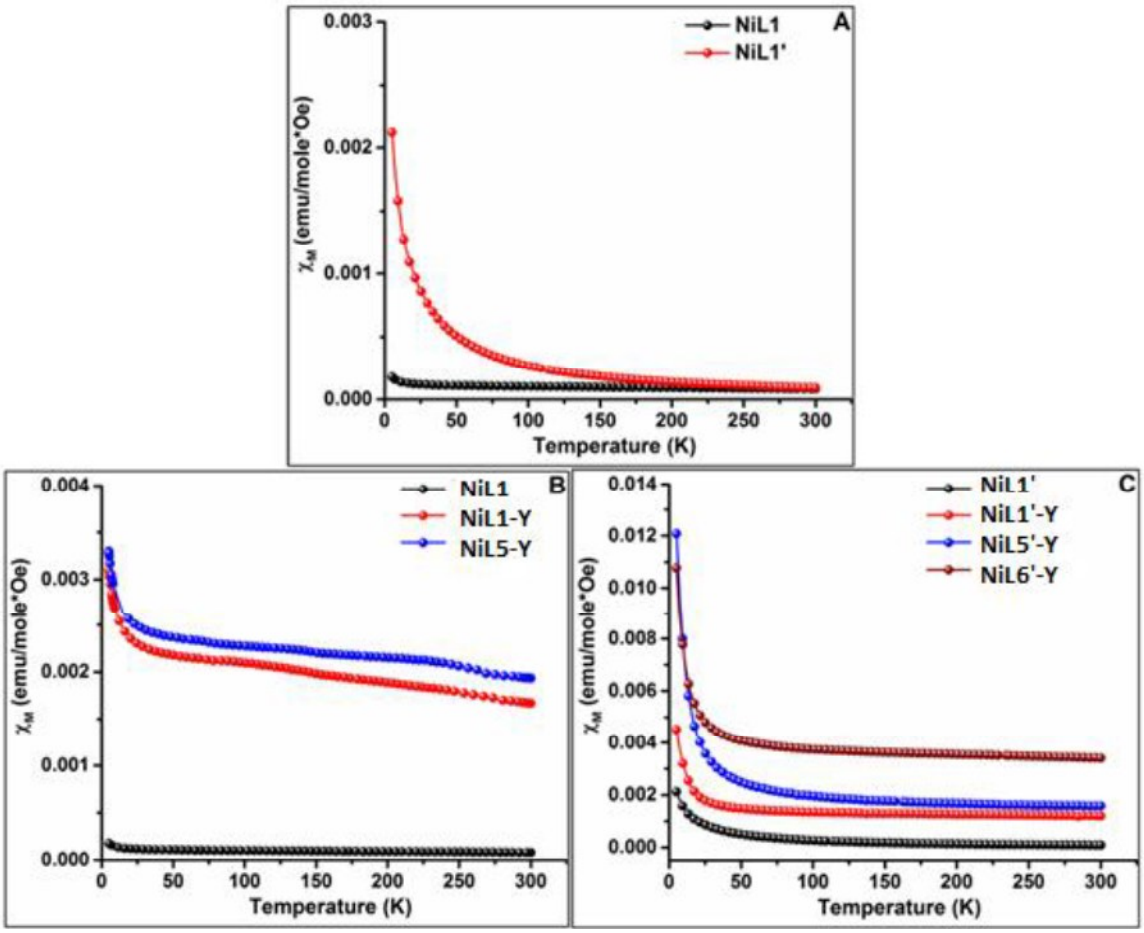

Figure 6.16: Molar susceptibility vs. temperature plots in the range of 5 K – 300 K of the complexes in free and encapsulated states (A) NiL1 and NiL1′, (B) NiL1, NiL1-Y and NiL5-Y and (C) NiL1′, NiL1′-Y, NiL5′-Y and NiL6′-Y.

6.2.10 Catalytic Study

All free-state and encapsulated nickel complexes have been employed for the phenol oxidation reaction. Observed catalysis results of all the complexes are shown in Table 6.7. The reaction conditions have been standardized with respect to encapsulated nickel salophen complex, NiL1-Y, with the varied amount of catalyst and at different reaction temperatures (Catalytic data given in Figure 6.17-6.18). All catalytic reactions are monitored by gas chromatography and % conversion calculated by using a calibration curve of phenol with bromobenzene as an internal standard (Figure 6.19).

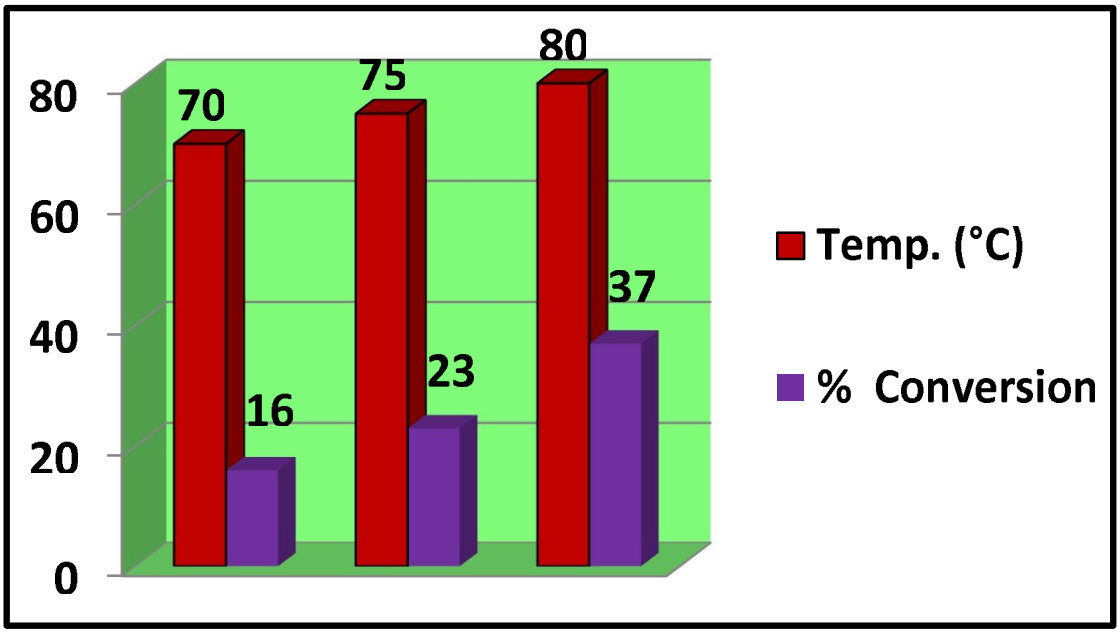

Figure 6.17: % Conversion of phenol oxidation with respect to temperature.

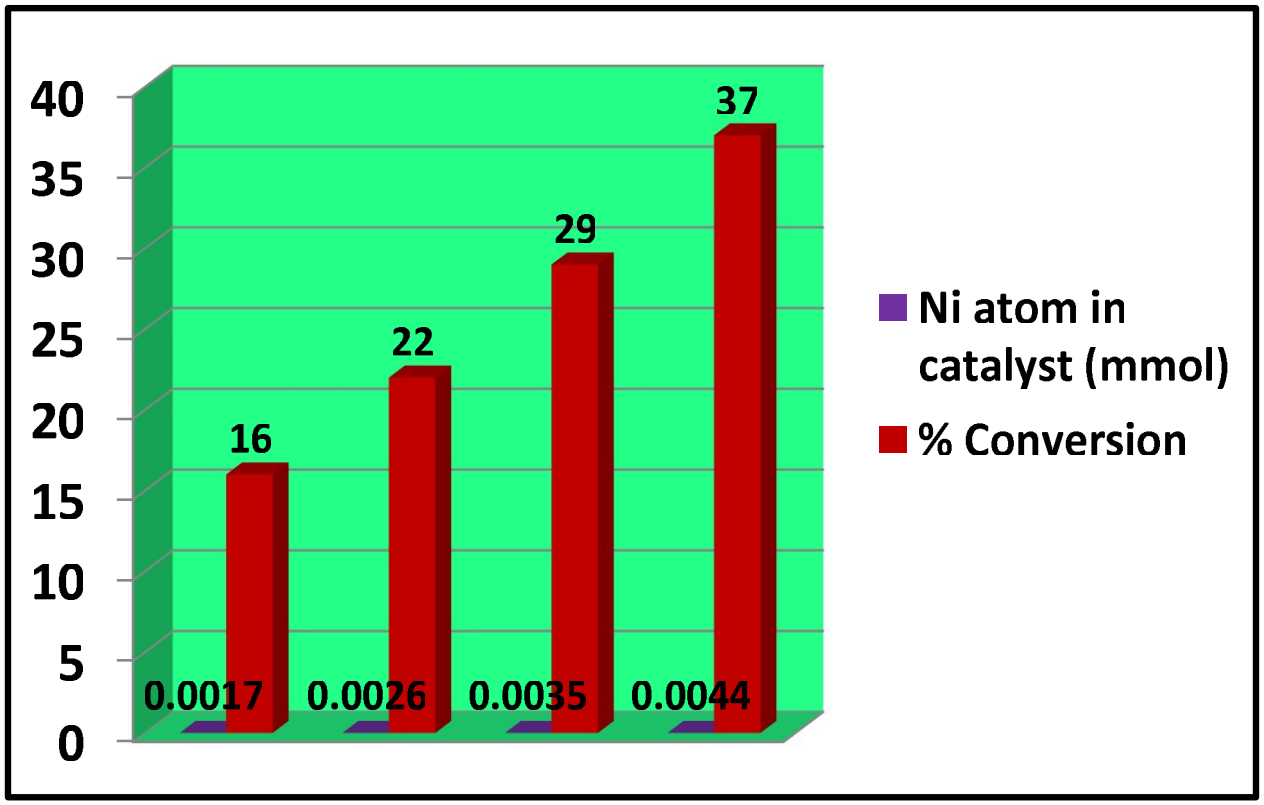

Figure 6.18: % Conversion of phenol oxidation with respect to amount of catalyst.

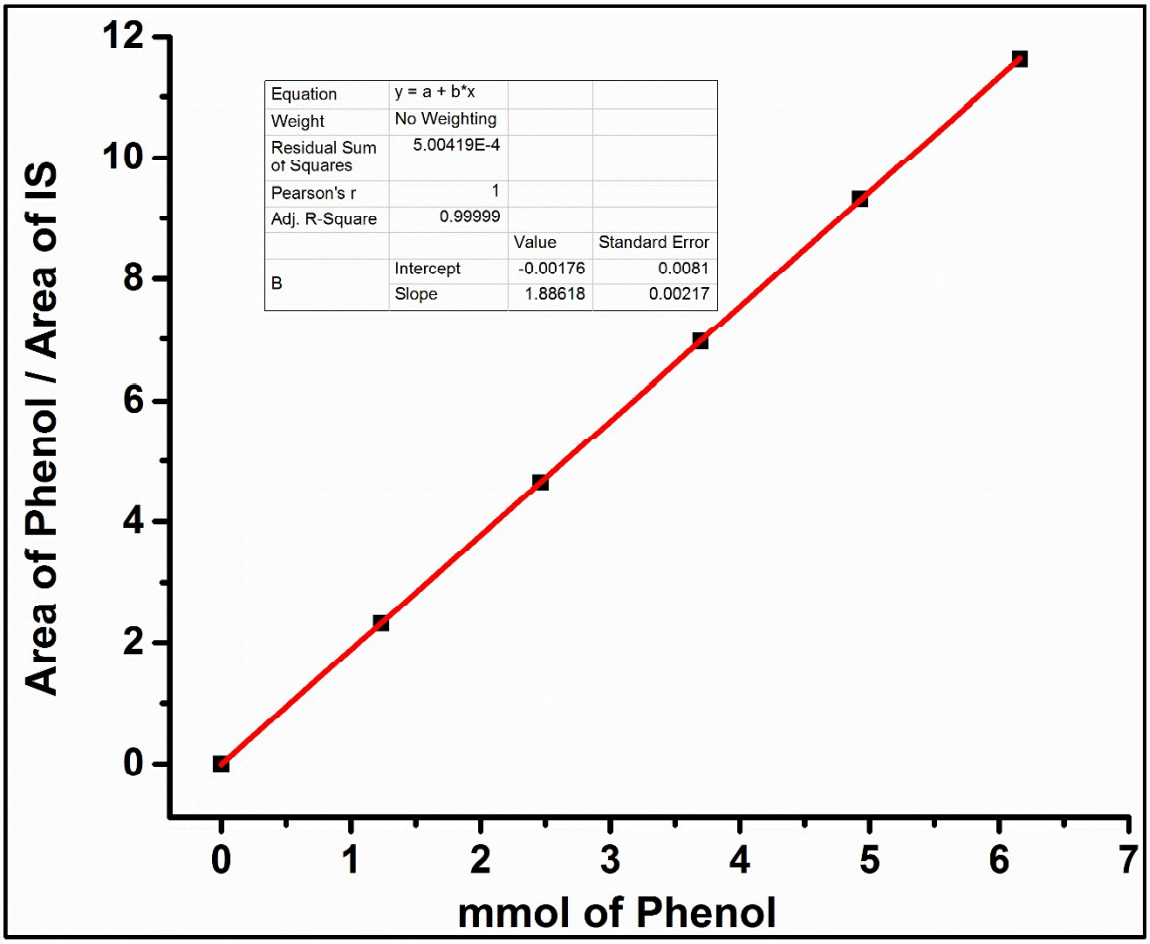

Figure 6.19: Calibration curve of phenol.

A plausible mechanism for the phenol oxidation reaction catalyzed by Ni(II) Schiff-base complexes is shown in Scheme 6.1. A reactive species (NiL--H_2O_2) is first generated as intermediate by the attack of H_2O_2 on the Ni(II) complex followed by quick generation of NiL*S (shown in the Scheme 6.1) species. Finally the catechol formation takes place by the transfer of oxygen from H_2O_2 to phenol with the simultaneous release of water molecule.[50]

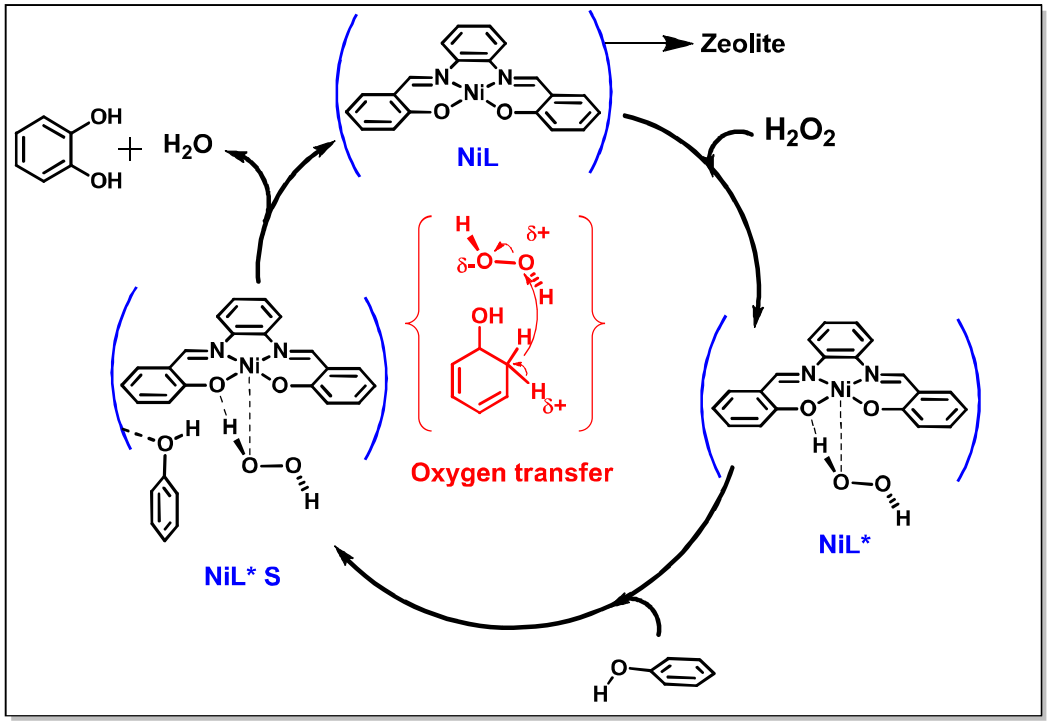

Scheme 6.1: A Plausible mechanism for conversion of phenol to catechol in the presence of nickel salophen complex and H_2O_2 (adapted from Ref.[50]).

All the complexes under encapsulation exhibit quite an enhanced catalytic activities as compared to their corresponding free states. Both free and encapsulated state complexes are more selective towards the formation of catechol over hydroquinone. However, free state complexes are marginally more selective for the catechol formation over the corresponding encapsulated states.

Table 6.7: Oxidation of phenol by nickel exchanged zeolite Y and neat and encapsulated nickel salophen complexes in presence of H_2O_2 as oxidant.

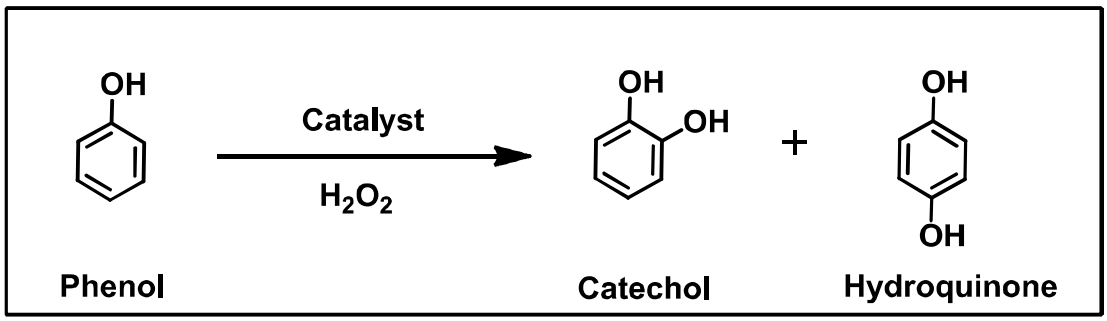

S. No	Samples	Ni^{+2} in catalyst (mmol)[a]	% Conversion	TON[b]	Selectivity	
					Catechol	Hydroquinone
1	**Zeolite-Y**	-	2	-	80	20
2	**Ni-Y**	0.01814	14	47.5	78	22
3	**NiL1**	0.06701	10	9.1	81	19
4	**NiL1-Y**	0.00443	37	514.6	75	25
5	**NiL1′**	0.06701	24	22.0	78	22
6	**NiL1′-Y**	0.00468	32	421.4	74	26
7	**NiL5**	0.05772	5	5.3	95	5
8	**NiL5-Y**	0.00460	43	576.1	72	28
9	**NiL5′**	0.05772	15	16.0	80	20
10	**NiL5′-Y**	0.00477	39	503.8	76	24
11	**NiL6**	0.05399	13	14.8	90	10
12	**NiL6-Y**	0.00383	33	531.0	78	22
13	**NiL6′**	0.05399	18	20.5	82	18
14	**NiL6′-Y**	0.00357	30	517.8	77	23

Reaction conditions: Phenol (0.58 g, 6.16 mmol), H_2O_2 (2.54 ml (30%), acetonitrile 2 ml, temperature 80 °C, catalyst (0.05 g for encapsulated complexes and 0.025 g for neat complexes), Reaction time-6 h.

[a] mmol of Ni atom calculated in 0.025 g for neat complexes and 0.05 g for encapsulated complexes).
[b] TON (turn over number): Turnover number calculated at the completion of reaction (mmol of phenol transformed / mmol of nickel metal in catalyst).

The direct comparison of catalytic results presented in this work with literature data is not very straight-forward as the measuring parameters could be many. The results and the conditions from these studies are

summarized in table 6.8. In terms of the parameters like amount of the catalyst used, time taken and % conversion, the catalyst of interest currently mentioned NiL5-Y competes well with other such catalysts.

Table 6.8: Comparison of zeolite based catalysts performances for the phenol hydroxylation reaction.[a]

Catalyst	Catalyst amount[b]	PhOH[c]	Time (h)	Conversion (%)[d]	Ref.
Ti-SBA-12	100	3:1	12	15.0	51
Fe(Hybe.2H_2O)Cl-Y	25	1:1	6	43.4	52
[Cr(Hybe)·2H_2O]Cl–Y	25	1:1	6	32.8	52
[Cu(sal-ambmz)Cl]-Y	25	1:3	6	42.0	53
$CuCl_{14}$Pc-NaY	750	2:1	8	21.4	54
Cu(NO_2)$_4$Pc-NaY	750	1:1	8	10.8	54
[Ni($Pic)_2$]-Y[e]	15	1:1	1.16	-	38
NiL5-Y	**50**	**1:3.6**	**6**	**43.0**	**This work**

[a]Oxygen source H_2O_2, solvent ACN, temperature 80°C, Hybe stands for 1,2-bis(2-hydroxybenzamido)ethane, sal-ambmz stands for (salicylaldehyde and 2-aminomethylbenzimidazole-based ligand), Pc stands for phthalocyanine and Pic stands for picolinato. [b] Catalyst amount in (mg). [c] PhOH/H_2O_2 molar ratio. [d] Conversion of PhOH (%). [e] Reaction mixture is subjected to microwave irradiation (280 W).

6.2.11 Structural modification and modified functionality

It is quite remarkable to note that the reactivity in terms of turn over numbers (TON) of all encapsulated complexes along with the Ni(II) exchanged zeolite Y are considerably higher than the all free state nickel complexes. A metal center in a complex, encapsulated inside the supercage of zeolite is categorized by isolation from the other metal centers by the host lattice and it has much lower mobility. Therefore, to achieve the desired reactivity, required reactive sites are much lesser inside the cavities, yielding higher TON.

To achieve the comparable and variable molecular dimensions of the transition metal Schiff-base complexes with that of the zeolite cavity and hence modified reactivity, attaching different substituents to the salophen Schiff-base ligand moiety could be a viable option. In this report, with encapsulation, structural and functional modifications of two different series of Ni(II) salophen complexes have been studied in details. Free-state Ni(II) sal-1,2-phen systems exhibit more planarity around metal center whereas the other series {Ni(II) sal-1,3-phen } show typical arrangement of the central phenyl ring (Figure 6.20) yielding a certain extent of non-planarity.[46] An interesting observation emerging from the electronic spectroscopic studies of the both series is associated with the metal-related transition; the transition for NiL1 complex (complex of Ni(II) sal-1,2-phen series) appears at 487 nm whereas that for NiL1′ complex (complex of Ni(II) sal-1,3-phen series) appears at 440 nm. These observations actually supports disrupted π delocalization around the metal for NiL1′ system, as studied previously.[46]

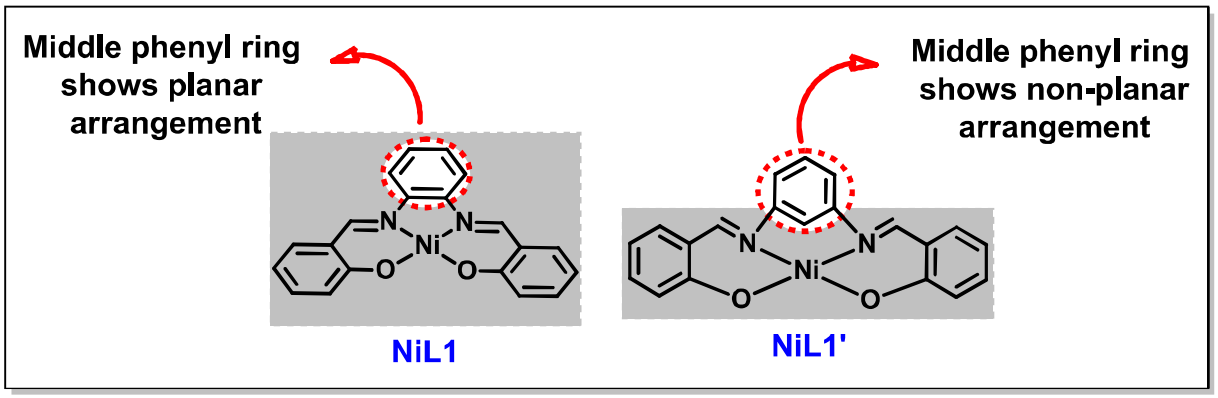

Figure 6.20: Representation of middle phenyl ring arrangement in both {Ni(II) sal-1,2-phen} and {Ni(II) sal-1,3-phen} complexes.

Magnetic studies also clearly indicate an extent of non-planarity around nickel metal center in [Ni(II) sal 1,3 phen] complexes (see Figure 6.16A). Planar electron–rich metal center becomes less susceptible for the nucleophilic attack of H_2O_2. Therefore, being more non-planar, the [Ni(II) sal-1,3-phen] systems show enhanced reactivity towards phenol oxidation as compared to the corresponding [Ni(II) sal-1,2-phen] systems. Apart from electronic and magnetic studies, XPS studies also indicate nickel center as more electropositive in NiL1′ complex as compared to that in NiL1 complex and more electropositive metal center acts as more efficient receptive center for the nucleophilic attack of hydrogen peroxide. With the same line of argument, free-state NiL6′ complex with $–NO_2$ group attached, is found to be the most active

catalyst for the phenol oxidation reaction (plausible mechanism for phenol oxidation shown in Scheme 6.1). In another series, NiL6 complex is most reactive however, though is still less reactive as compared to the NiL6′ complex.

All the encapsulated nickel complexes exhibit much higher reactivity in comparison to their neat analogues. At this point, it is quite interesting to note that Ni-exchanged zeolite shows better reactivity as compared to all the free-state complexes (Catalysis Table 6.7). Substantial reactivity of Ni-exchanged zeolite indeed identifies the Ni(II) center is the catalytic center and active site isolation in the supercage of zeolite-Y as major driving factor for enhancing the reactivity. Encapsulation of Ni(II) salophen systems inside the cavities of zeolite-Y primarily introduces site isolation and with an extent of distortion it makes the metal center further electropositive and subsequently more reactive. Interestingly, encapsulated L series complexes are found with more improvement in the reactivity than corresponding complexes of L′ series. Once encapsulated, encapsulation indeed provides site isolation very similarly for both the series. Therefore, marginal difference in the reactivity is by and large controlled by the different structural modification that these two series undergo on encapsulation. Non-planar arrangement of the central benzene ring in free-state non-planar Ni complexes of L′ series actually is enforced for improved planarity on encapsulation. Encapsulated complexes of L′ series encounter typically more enhancement of electron density on the central metal compared to L series complexes.[46] These structural modifications, well-supported by the electronic spectroscopic data, controls the catalytic activities marginally here. All encapsulated [Ni(II) sal-1,3-phen] systems show red shift in metal-related transition as compared to their free-state analogues whereas all [Ni(II) sal-1,2-phen] systems show blue shift of same transition upon encapsulation. Therefore, the performance of the encapsulated catalysts, is governed by the major crucial factor like active site isolation, though electronic factor of the substituent groups, steric constraint imposed by the host framework also contribute towards catalytic activity. The overall comparative studies indeed, validate the mechanism of the phenol oxidation reaction.

The most striking result is observed for NiL5 system. Encapsulated NiL5 complex manifests maximum reactivity for the phenol oxidation reaction whereas its neat state is least reactive amongst the all entries in the Table 6.7. On encapsulation, TON of NiL5 complex increases from 5.3 to 576.1. In the free-state NiL5 complex, electron donating character of the substituent –OCH_3 group prevails to make the catalyst least efficient in the lot. The electropositive character of the nickel metal increases due to non-planarity

induced by steric constraint inside the host cavity. The effect is more pronounced when large substituent such as -OCH_3 on salophen is added on ligand moiety to finally enhance the molecular dimension of complex. The, degree of non-planarity is higher in case of NiL5 complex within the supercage. Subsequently, the nickel center becomes more electron deficient, resulting amazingly higher reactivity. XPS analysis of encapsulated systems confirms enhanced electropositive character of the nickel metal center.

A very recent literature report states that in -situ generation of uniform peroxo species permit an unusual non-radical reaction mechanism for the oxidation reaction in presence of H_2O_2 as oxidant in zeolite framework. These species play a crucial role for the superior reactivity of catalysts towards H_2O_2 based hydroxylation.[55] Active and stable M-OOH species is generated inside the supercage of zeolite-Y and formation of M-OOH species is identified as the rate determining step for the H_2O_2 based oxidation reaction.[56] Phenol is then actually adsorbed on the surface of zeolite, but not at catalytic metal center to finally be oxidized. Zeolite walls eventually make phenol coming to the close proximity of the catalytic center which facilitates the completion of the reaction. Few of the earlier reports have explored the catalytic activity of the Ni-salen complexes encapsulated in zeolite -Y for styrene oxidation reaction.[41, 57] The enhancement of the catalytic activity of these encapsulated complexes are mainly controlled by the steric constraints that the complexes undergo on encapsulation. Structure of the catalyst and subsequently electronic distribution becomes the decisive factor as styrene gets attached to the catalytic metal center and hence site isolation is not so important for that matter. Phenol oxidation reaction however, is facilitated via site isolation and hence is fundamentally following different mechanistic pathways from styrene oxidation.

6.3 CONCLUSION

Two small series of Ni(II) Schiff-base complexes [Ni(II) sal-1,2-phen and Ni(II) sal-1,3-phen series] have been synthesized in neat as well as in encapsulated states. All the systems are successfully characterized by the help of several spectroscopic techniques such as XRD, SEM-EDS, BET, XPS, IR, UV-Vis studies and thermal analysis, magnetic studies and further employed as catalysts for the oxidation of phenol in presence of H_2O_2 as oxidant. Electronic behavior of the neat and encapsulated systems is analyzed the help of UV-Vis and XPS studies. The complexes of [Ni(II) sal-1,3-phen] series are proven to have non-

planarity in their free states and as a result, formation of more electropositive nickel center becomes the basis of the marginally better reactivity towards phenol oxidation as compared to the [Ni(II) sal-1,2-phen] series. Zeolite supercage imposes notable space constraint when the guest complex has comparable molecular dimensions with that of the supercage. Hence, the efficiency of the catalysts is improved. The plausible driving factors for the betterment of reactivity of the complexes could be the altered coordination environment around metal center as well as isolation of active sites inside the cavities of zeolite. The comparative scrupulous analysis actually concludes that the phenol oxidation reaction is rather facilitated due to the site isolation phenomenon imparted by the heterogeneous catalysis.

6.4 REFERENCES

1. M. Mandal, V. Nagaraju, B. Sarma, G. Karunakar and K. K. Bania, *ChemPlusChem*, 2015, **80**, 749-761.
2. S. Rayati, E. Bohloulbandi and S. Zakavi, *Inorg. Chem. Commun.*, 2015, **54**, 38-40.
3. J. P. Mehta, D. K. Parmar, D. R. Godhani, H. D. Nakum and N. C. Desai, *J. Mol. Catal. A: Chem.*, 2016, **421**, 178-188.
4. R. Abraham and K. K. M. Yusuff, *J. Mol. Catal. A: Chem.*, 2003, **198**, 175-183.
5. C. Jin, W. Fan, Y. Jia, B. Fan, J. Ma and R. Li, *J. Mol. Catal. A: Chem.*, 2006, **249**, 23-30.
6. A. Primo and H. Garcia, *Chem. Soc. Rev.*, 2014, **43**, 7548-7561.
7. Z. L. You, H. L. Zhu and W. S. Liu, *Z. Anorg. Allg. Chem*, 2004, **630**, 1617-1622.
8. Z. L. You and H. L. Zhu, *Z. Anorg. Allg. Chem*, 2004, **630**, 2754-2760.
9. A. Golcu, M. Tumer, H. Demirelli and R. A. Wheatley, *Inorg. Chim. Acta*, 2005, **358**, 1785-1797.
10. K. E. Splan, A. M. Massari, G. A. Morris, S. S. Sun, E. Reina, S. T. Nguyen and J. T. Hupp, *Eur. J. Inorg. Chem.*, 2003, **2003**, 2348-2351.
11. G. A. Morris, H. Zhou, C. L. Stern and S. T. Nguyen, *Inorg. Chem.*, 2001, **40**, 3222-3227.
12. W.-K. Dong, Y.-X. Sun, Y.-P. Zhang, L. Li, X.-N. He and X.-L. Tang, *Inorg. Chim. Acta*, 2009, **362**, 117-124.
13. M. Nielsen, N. B. Larsen and K. V. Gothelf, *Langmuir*, 2002, **18**, 2795-2799.
14. R. Noyori, M. Aoki and K. Sato, *Chem. Commun.*, 2003, 1977-1986.
15. B. S. Lane and K. Burgess, *Chem. Rev.*, 2003, **103**, 2457-2474.
16. H. Nemoto, T. Nishiyama and S. Akai, *Org. Lett.*, 2011, **13**, 2714-2717.
17. H. Nohl, W. Jordan and R. J. Youngman, *Adv. Free Radical Biol. Med.*, 1986, **2**, 211-279.
18. G. A. Hamilton, J. W. Hanifin Jr and J. P. Friedman, *J. Am. Chem. Soc.*, 1966, **88**, 5269-5272.
19. J. Varagnat, *Ind. Eng. Chem. Prod. Res. Dev.*, 1976, **15**, 212-215.
20. M. A. Brook, L. Castle, J. R. L. Smith, R. Higgins and K. P. Morris, *J. Chem. Soc., Perkin Trans. 2*, 1982, 687-692.
21. F. Chioccara, P. Di Gennaro, G. La Monica, R. Sebastiano and B. Rindone, *Tetrahedron*, 1991, **47**, 4429-4434.
22. S. Goldstein, G. Czapski and J. Rabani, *J. Phys. Chem.*, 1994, **98**, 6586-6591.
23. R. Yu, F.-S. Xiao, D. Wang, J. Sun, Y. Liu, G. Pang, S. Feng, S. Qiu, R. Xu and C. Fang, *Catal. Today*, 1999, **51**, 39-46.
24. J. Sun, X. Meng, Y. Shi, R. Wang, S. Feng, D. Jiang, R. Xu and F.-S. Xiao, *J. Catal.*, 2000, **193**, 199-206.
25. M. Maurya, S. Titinchi, S. Chand and I. Mishra, *J. Mol. Catal. A: Chem.*, 2002, **180**, 201-209.

26. A. Dubey, V. Rives and S. Kannan, *J. Mol. Catal. A: Chem.*, 2002, **181**, 151-160.
27. V. Mouarrawis, R. Plessius, J. I. van der Vlugt and J. N. H. Reek, *Front Chem*, 2018, **6**, 623-623.
28. A. Uzun, V. A. Bhirud, P. W. Kletnieks, J. F. Haw and B. C. Gates, *J. Phys. Chem. C*, 2007, **111**, 15064-15073.
29. Y. Umemura, Y. Minai and T. Tominaga, *J. Phys. Chem. B*, 1999, **103**, 647-652.
30. M. Mandal, V. Nagaraju, G. V. Karunakar, B. Sarma, B. J. Borah and K. K. Bania, *J. Phys. Chem. C*, 2015, **119**, 28854-28870.
31. G. R. Reddy, S. Balasubramanian and K. Chennakesavulu, *J. Mater. Chem. A*, 2014, **2**, 15598-15610.
32. K. K. Bania and R. C. Deka, *J. Phys. Chem. C*, 2012, **116**, 14295-14310.
33. V. K. Bansal, P. P. Thankachan and R. Prasad, *Appl. Catal., A*, 2010, **381**, 8-17.
34. G. Ramanjaneya Reddy, S. Balasubramanian and K. Chennakesavulu, *J. Mater. Chem. A*, 2014, **2**, 15598-15610.
35. I. Kuźniarska-Biernacka, K. Biernacki, A. L. Magalhães, A. M. Fonseca and I. C. Neves, *J. Catal.*, 2011, **278,** 102-110.
36. M. Moosavifar, S. Tangestaninejad, M. Moghadam, V. Mirkhani and I. Mohammadpoor-Baltork, *J. Mol. Catal. A: Chem.*, 2013, **377**, 92-101.
37. M. R. Maurya, P. Saini, C. Haldar, A. K. Chandrakar and S. Chand, *J. Coord. Chem.*, 2012, **65**, 2903-2918.
38. K. K. Bania and R. C. Deka, *J. Phys. Chem. C*, 2013, **117**, 11663-11678.
39. M. Jafarian, M. Rashvand avei, M. Khakali, F. Gobal, S. Rayati and M. Mahjani, *J. Phys. Chem. C*, 2012, **116**, 18518-18532.
40. A. Choudhary, B. Das and S. Ray, *Dalton Trans.*, 2015, **44**, 3753-3763.
41. A. Choudhary, S. Kumari and S. Ray, *ACS Omega*, 2017, **2**, 6636-6645.
42. W. H. Quayle, G. Peeters, G. L. De Roy, E. F. Vansant and J. H. Lunsford, *Inorg. Chem.*, 1982, **21**, 2226-2231.
43. H. S. Abbo and S. J. Titinchi, *Top. Catal.*, 2010, **53**, 1401-1410.
44. C. B. Vidal, G. S. Raulino, A. L. Barros, A. C. Lima, J. P. Ribeiro, M. J. Pires and R. F. Nascimento, *J. Environ. Manage.*, 2012, **112**, 178-185.
45. D. R. Godhani, H. D. Nakum, D. K. Parmar, J. P. Mehta and N. C. Desai, *J. Mol. Catal. A: Chem.*, 2016, **415,** 37-55.
46. S. Kumari, K. Maddipoti, B. Das and S. Ray, *Inorg. Chem.*, 2019, **58**, 1527-1540.
47. X. Cai, H. Wang, Q. Zhang, J. Tong and Z. Lei, *J. Mol. Catal. A: Chem.*, 2014, **383**, 217-224.
48. W. H. Quayle and J. H. Lunsford, *Inorg. Chem.*, 1982, **21**, 97-103.
49. D. N. Stamires and J. Turkevich, *J. Am. Chem. Soc.*, 1964, **86**, 749-757.
50. C. K. Modi and P. M. Trivedi, *Microporous Mesoporous Mater.*, 2012, **155**, 227-232.
51. A. Kumar and D. Srinivas, *J. Mol. Catal. A: Chem.*, 2013, **368**, 112-118.
52. M. R. Maurya, S. J. Titinchi and S. Chand, *J. Mol. Catal. A: Chem.*, 2004, **214**, 257-264.
53. M. R. Maurya, A. K. Chandrakar and S. Chand, *J. Mol. Catal. A: Chem.*, 2007, **263**, 227-237.
54. R. Raja and P. Ratnasamy, *Appl. Catal., A*, 1996, **143**, 145-158.
55. Y. Zhou, Z. Ma, J. Tang, N. Yan, Y. Du, S. Xi, K. Wang, W. Zhang, H. Wen and J. Wang, *Nat. Commun.*, 2018, **9**, 2931.
56. S. Yamaguchi, A. Suzuki, M. Togawa, M. Nishibori and H. Yahiro, *ACS Catal.*, 2018, **8**, 2645-2650.
57. A. Choudhary, B. Das and S. Ray, *Dalton Trans.*, 2016, **45**, 18967-18976.